Université du Québec à Montréal

Effect of Environmental Temperature Variations on Silicon Ring-based Wavelength and Mode Multiplexers

A Dissertation

Submitted to the Faculty of Graduate Studies in Partial

Fulfillment of the Requirements for the Degree of

Master in Electrical Engineering

By

Hoda Rezaei

October 2022

UNIVERSITÉ DU QUÉBEC À MONTRÉAL

EFFET DES VARIATIONS DE TEMPÉRATURE SUR L'ANNEAU MULTIPLEXEURS DE LONGUEUR D'ONDE ET DE MODE

MÉMOIRE PRÉSENTÉ
COMME EXIGENCE PARTIELLE
DE LA MAÎTRISE EN GÉNIE ÉLECTRIQUE

PAR
HODA REZAEI

OCTOBRE 2022

Acknowledgements

I would like to take this opportunity to express my extreme gratitude to my supervisor, Professor Michaël Ménard. His outlook and confidence inspired me; During a challenging time in my studies, I profited from his advice at many stages of this research project. I especially want to thank him for his patience when I was confused.

Contents

List of Figures

List of Tables

List of Abbreviations

SOI	Silicon on Insulator
PIC	Photonics Integrated Circuit
WDM	Wavelength Division Multiplexing
MDM	Mode Division Multiplexing
DWDM	Dense Wavelength Division Multiplexing
CWDM	Corse Wavelength Division Multiplexing
FWM	Four-wave mixing
SPM	Self-Phase Modulation
XPM	Cross-Phase Modulation
MRR	Micro-Ring Resonator
RTR	Racetrack Resonator
ER	Extinction Ratio
TE	Transverse Electric
Q factor	Quality factor
BER	Bit Error Rate
ADC	Asymmetric Directional Coupler
MZI	Mach-Zehnder Interferometer
AWG	Array Waveguide Grating
PV	Process Variations
TM	Transverse Magnetic
APF	All-Pass Filter
ADF	Add-Drop Filter
Free Spectral Range	FSR
IL	Insertion Loss
RL	Return Loss
Full Width at Half Maximum	FWHM

Résumé

Au cours des dernières décennies, le multiplexage par répartition en longueur d'onde (WDM) est devenu une technologie clé pour fournir une capacité de transmission èlevée et une large bande passante pour les réseaux de télécommunication. De plus, le WDM fonctionne dans un régime monomode tout en offrant une évolutivité limitée par la bande passante des amplificateurs optiques. Le multiplexage par répartition en mode (MDM), une nouvelle technique compatible avec le multiplexage par répartition en longueur d'onde, a été introduit pour résoudre ce problème. Cette technologie permet d'augmenter la capacité des systèmes de télécommunications optiques tout en obtenant de larges bandes passantes agrégées car elle fonctionne avec plusieurs modes.

Dans ce mémoire, deux multiplexeurs à 4 canaux basés sur des microanneaux de silicium ont été simulés: un démultiplexeur WDM capable de combiner des canaux définis sur la grille ITU de 200 GHz fonctionnant avec le mode fondamental et un multiplexeur MDM fonctionnant avec les modes TE_0 à TE_3. L'objectif principal de ce mémoire est d'ètudier l'effet des changements de température sur les deux multiplexeurs. Des simulations dans lesquelles la température était variée ont été réalisées avec les deux systèmes pour déterminer quelle technique de multiplexage est la plus sensible aux changements thermiques.

Mots clés: microanneau de silicium, résonateur de circuit, multiplexage par répartition en longueur d'onde, multiplexage par répartition en mode, effet des variations de température

Abstract

Over the last decades, Wavelength Division Multiplexing (WDM) has emerged as a key technology for providing high transmission capacity and wide bandwidth for telecommunication networks. Furthermore, WDM operates in a single-mode regime while providing scalability limited by the bandwidth of optical amplifiers. Mode Division Multiplexing (MDM), a new technique compatible with wavelength-division multiplexing, has been introduced to address this issue. This technology allows for increased capacity of optical telecommunication systems while achieving large aggregate bandwidths as it operates with multiple modes.

In this dissertation, two 4-channel multiplexers based on silicon micro-rings were simulated: a WDM demultiplexer capable of combining channels defined on the ITU 200 GHz grid operating in the fundamental mode and an MDM multiplexer operating with the TE_0 to TE_3 modes. The main goal of this thesis is to study the effect of changes in temperature on both multiplexers. Simulations in which the temperature was varied were performed with both systems to determine which multiplexing technique is most sensitive to thermal changes.

Keywords: silicon micro-ring, racetrack resonator, wavelength division multiplexing, mode division multiplexing, temperature variations effect

Chapter 1

Introduction

1.1 Silicon Photonics

Silicon photonics has garnered special attention due to its compatibility with CMOS fabrication processes, low propagation loss, low-cost large-scale fabrication, and high-performance circuits (Mulcahy et al., 2022; Yuan et al., 2021; Yan et al., 2021; Besancon et al., 2021; Gautam et al., 2014). Furthermore, it enables an immense array of photonic components, including filters, modulators, photodetectors, (de)multiplexers, splitters, optical attenuators, and polarization rotators. Silicon-on-insulator (SOI) refers to wafers widely used in the electronic industry (Mulcahy et al., 2022; Gautam et al., 2014). In SOI platforms, a crystalline silicon layer is bonded onto an oxidized silicon substrate. The high index contrast between the layers of silicon core (n_{si}=3.45) and the oxide cladding (n_{sio2}=1.44) leads to strong mode confinement in the core, which allows the production of compact SOI photonic integrated circuits (PICs) (Lin et al., 2022). This results in several benefits such as compact nanowires with tight bending radii and reduced field penetration (Mistry, 2020; Zheng et al., 2022; Liu et al., 2021).

Accordingly, silicon photonics has found applications in transceivers for data centers and even long-haul networks. However, the need for high telecommunication bandwidths is not limited to these controlled environments. For instance, there is a growing interest in developing optical interconnects for space applications. Furthermore, even in these harsh environment applications, transmission capacities of several hundreds of Gb/s are needed. Although transmission capacities of up to 800

Gb/s per channel are commercially available, these systems rely on coherent detection, which require sensitive and expensive narrow linewidth lasers with precise phase control. Therefore, in this study, the focus is put on channel multiplexing techniques to increase the optical link capacity. More specifically, we consider the well establishing wavelength division multiplexing (WDM) technique and the emerging mode division multiplexing (MDM) approach. Both are described in more details below. Our goal is to identify which one is more suitable for harsh environment applications by comparing the effect that temperature changes have on the performance of typical silicon photonic multiplexers implemented with ring resonators.

1.2 WDM Optical (De)Multiplexing

The recent need for high-speed internet connections has led to the emergence of wide bandwidth communication networks (Sayed et al., 2021). Bandwidth development has become crucial, which has led to the deployment of Wavelength Division Multiplexing (WDM) technology. In WDM, multiple optical carriers are combined into a single fiber (Rai & Garg, 2021). These propagating optical carriers collected in the single fiber must then be demultiplexed at the receiver. Transmitting multiple wavelengths via a single optical fiber enables a higher data-transfer rate (Mistry, 2020).

WDM networks are categorized into two categories: Dense Wavelength Division Multiplexing (DWDM) and Corse Wavelength Division Multiplexing (CWDM). The notable difference between DWDM and CWDM is the channel spacing. Currently, in DWDM networks, channels are placed 0.8 nm apart, whereas in CWDM networks they are placed 20 nm apart (Mistry, 2020). Thus, in the far denser DWDM network, the greater number of channels enable transmission of more optical carriers, which is especially suitable for long-reach communications. On the other hand, CWDM is commonly used for short-reach communications. Consequently, large bandwidths are obtained with WDM networks with high channel capacities and data-transfer rates (Sayed et al., 2021).

However, certain physical phenomena significantly limit WDM performance, such as nonlinear effects, dispersion, and attenuation (Rai & Garg, 2021). Attenuation occurs when the electromagnetic field traveling through an optical fiber scatters out-side the fiber. Nonlinear phenomena, such as four-wave mixing (FWM), self-phase modulation (SPM), and cross-phase modulation (XPM) can also negatively impact WDM performance. By supporting multiple channels spaced as densely as possible, WDM networks are susceptible to FWM resulting from interactions between the numerous optical signals in the fiber. Unequal channel spacing can be used to diminish the effect of FWM.

1.3 MDM-WDM Optical (De)Multiplexing

Despite its advantages, wavelength division multiplexing has limitations due to channel spacing and crosstalk caused by optical nonlinearity (Bagheri & Green, 2009). In particular, single-mode optical components face capacity limits; hence, there has been significant interest in other multiplexing techniques. Mode division multiplexing (MDM) emerged from the fast-increasing demand for high transmission capacity in fiber communication networks and on-chip optical interconnects (Zheng et al., 2018; Qiu et al., 2017). The motivation behind MDM is higher capacity and overcoming the scaling issue by operating in the multimode regime. In this method, each mode acts as an independent special channel. In principle, higher-order modes can increase the number of channels for data transmission in on-chip optical multiplexers and increase design flexibility (Li et al., 2019; Ding et al., 2014). In many implementations of mode multiplexing, multiple optical signals are modulated and then transferred to a multimode waveguide. However, transferring information to multimode optical carriers is complex; therefore, it is seldom considered in integrated photonics (Jia et al., 2019; Luo et al., 2014). Mode division multiplexing based on a single wavelength has advantages with regards to cost and compatibility with other multiplexing technologies (Zhou et al., 2018). MDM-WDM is desirable as it can increase system capacity.

1.4 Objectives and Contributions

As explained above, two different solutions are becoming available to implement optical links with large capacities: WDM, which is a well-established and commercially available solution, and MDM, which has attracted a lot of attention in the research community for its capability to generate multiple channels with a single source. Nevertheless, unlike for WDM, there are very few studies addressing the effect of temperature variations on MDM devices. Furthermore, as optical links make their way into harsh environments, such as space applications, it will become necessary to access which multiplexing technology provides the most benefits in these conditions. The work presented here is a first step to fill this gap in the scientific literature. The main purpose of this study is to identify which multiplexing approach is the most susceptible to environmental temperature changes when they are implemented with similar technology. This comparative study is the first of its kind and is based on a widely used device in both WDM and MDM multiplexers: silicon micro-ring resonators. To realize this, the following three objectives were completed:

- First, design a four-channel WDM demultiplexer following the 200 GHz ITU grid based on cascaded symmetric micro-ring resonators operating in the fundamental mode.
- Second, design a four-channel MDM multiplexer combining multiple TE modes based on cascaded asymmetric racetrack resonators. This device should support four TE modes.
- Third, investigate the effect of changes in temperature on both multiplexers to find out which one is more sensitive to environmental temperature variations.

The realization of these objectives led to the demonstration that ring-based mode multiplexers are more sensitive to temperature variations than their WDM counterpart. This can have important implications when making a decision about the optimal architecture of high bandwidth optical telecommunication links for harsh environments. This contribution was presented at the Photonics North conference:

Hoda Rezaei and Michaël Ménard. 2022 “Thermal Performance Comparison of Silicon Ring-based WDM and MDM Multiplexers” presented at Photonics North, Niagara Falls, Canada.

1.5 Outline of the Thesis

This thesis comprises seven chapters organized as follows.

Chapter 1 is the introduction.

Chapter 2 addresses the fundamental of mode theory, directional couplers, multimode waveguides, and ring resonators. A brief description of prominent features such as crosstalk and Quality factor (Q factor) is presented.

In Chapter 3, a literature review of WDM and MDM based on MZIs, ring resonators, and directional couplers is presented.

Chapter 4 describes the four-channel silicon ring-based WDM demultiplexer, including its architecture, optical specifications, and simulated responses.

Chapter 5 presents the four-channel silicon racetrack-based MDM multiplexer. This chapter includes the simulated configuration, the relevant optical characteristics, and our results.

In Chapter 6, we provide the results on the investigation about the effect of temperature changes on the two simulated optical multiplexers.

Chapter 7 discusses our conclusions.

Chapter 2

Theory

2.1 Optical Modes in Waveguides

The structure of a waveguide includes a core enveloped by a cladding or substrate where the optical signal is confined in the core through total internal reflection when the propagation angle Φ does not exceed the critical angle. Additionally, the propagation angle of the light must meet the phase-matching condition, which is described by the following equation:

$$\tan(kn_1 a \sin\Phi - \frac{m\pi}{2}) = \sqrt{\frac{2\Delta}{\sin^2\Phi} - 1} \tag{2.1}$$

where a is the core radius, which shows that the propagation angle is dependent of the waveguide structure, kn_1 is the wavenumber of light in the core, and Δ is the relative refractive index difference ($\Delta = \frac{{n_1}^2 - {n_0}^2}{2{n_1}^2}$) between the core ($n_1$) and the cladding ($n_0$). Under this condition, the electric fields resulting from reflections inside the waveguide interfere constructively. The field distribution that satisfies the phase-matching condition is known as a mode. In Eq. 2.1, m is the number identifying the order of the propagating modes where the mode with the minimum propagation angle is the fundamental mode ($m = 0$), and other modes with larger propagation angles are known as higher-order modes ($m > 0$)(Heebner et al., 2008; Okamoto, 2021). The phase-matching condition can be rewritten as:

$$kn_1 a\sqrt{2\Delta} = \frac{\cos^{-1}\zeta + \frac{m\pi}{2}}{\zeta} \quad , \quad \zeta = \frac{\sin\Phi}{\sqrt{2\Delta}} \tag{2.2}$$

where ζ is normalized to one and $\nu = kn_1a\sqrt{2\Delta}$ is the normalized frequency. In this case, the propagation characteristics of the waveguide can be calculated independently of the waveguide structure. The relation between the normalized frequency ν and ζ (which is equivalent to the propagation constant β) is called the dispersion equation, which gives the number of guided modes in the waveguide. The frequency at which the waveguide supports a single mode is called the cutoff frequency ν_c. When $\nu < \nu_c$ higher-orders are not guided. The cutoff wavelength λ_c is given by the equation:

$$\lambda_c = \frac{2\pi}{\nu_c} a n_1 \sqrt{2\Delta} \tag{2.3}$$

For a mode to be guided, the following condition should be satisfied:

$$n_0, n_s < \frac{\beta}{k} < n_1 \tag{2.4}$$

where $\frac{\beta}{k}$ is the independent dimension known as the effective index, and n_1, n_0 and n_s are the refractive indexes of the core, cladding, and substrate, respectively. Note that if $n_0, n_s < \frac{\beta}{k}$ the electromagnetic field radiates at the boundary of the core and cladding or substrate. Furthermore, the index variation as a function of wavelength ($\frac{dn}{d\lambda}$) indicates how much chromatic dispersion is present. The case when $\frac{dn}{dk} = 0$ is called no dispersion, $\frac{dn}{dk} < 0$ is called normal dispersion, and $\frac{dn}{dk} > 0$ is called anomalous dispersion (Steck, 2006).

2.2 Polarization

The polarization of a mode is defined by the orientation of its electric and magnetic fields. When the dominant electric field propagating inside a waveguide is perpendicular to the direction of propagation (usually oriented along the z-axis), it is known as a Transverse Electric (TE) mode. On the other hand, when the dominant propagating magnetic field is perpendicular to the z-axis, the electromagnetic field is known as a Transverse Magnetic (TM) mode (Okamoto, 2021).

2.3 Codirectional Couplers

The two parallel waveguides close to each other form is known as a directional coupler, as illustated in Fig. 2.1, and can be implemented in a horizontal or vertical arrangement (Bogaerts et al., 2012) where the optical eigenmodes of the first waveguide interfere with that of the second waveguide (Okamoto, 2021). Meanwhile, a fraction of the power of the input is coupled to the second waveguide, depending on the waveguide geometry and the gap between them. In other words, the coupling coefficient (k) can be controlled by adjusting the waveguide length and the distance between the two waveguides.

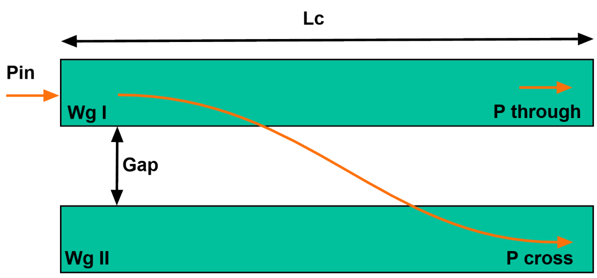

Figure 2.1: Model of a horizontal directional coupler showing the power transfer between two parallel waveguides.

The propagation constant difference between the two waveguides is expressed by

$$\delta = \frac{\beta_1 - \beta_2}{2} \tag{2.5}$$

where

$$\beta_1 = \frac{2\pi n_1}{\lambda} \quad , \quad \beta_2 = \frac{2\pi n_2}{\lambda} \tag{2.6}$$

and the propagation constant depends on the effective index of the related eigenmode. For most of codirectional couplers $k_1 = k_2$, which is obtained when the difference in propagation constants is zero $(\beta_1 = \beta_2, \delta = 0)$ and the two waveguides are sufficiently separated. The power coupling from waveguide 1 to waveguide 2 reaches 100% when the two propagation constants are equal and their length corresponds to the coupling length (Lc):

$$Lc = \frac{\pi}{2\sqrt{k^2+\delta^2}} = \frac{\pi}{2k} = \frac{\lambda}{2\Delta n} \tag{2.7}$$

where Δn is the difference between the effective indices of the waveguide ($\Delta n = n_1 - n_2$). Notably, the fraction of the power coupled from waveguide 1 to waveguide 2 is given by

$$\frac{P_{cross}}{P_0} = \sin^2(k.Lc) \tag{2.8}$$

where P_0 is the input optical power and P_{cross} is the coupled power traveling into the second waveguide.

Furthermore, the power remaining into the original waveguide is defined by:

$$\frac{P_{through}}{P_0} = \cos^2(k.Lc) \tag{2.9}$$

As mentioned above, the power in the modes can transfer between the waveguides. However, the power becomes concentrated in the second waveguide after a π phase shift between the two. Figure 2.2(a) shows the directional coupler length versus the coupler gap for the power to be coupled in the second waveguide. Figure 2.2(b) shows the coupling coefficient versus the gap for different coupling lengths. This plot is helpful in defining the main parameters of the coupling region in micro-ring resonators. It also demonstrates that it is possible to achieve the same coupling coefficient with different lengths and gaps.

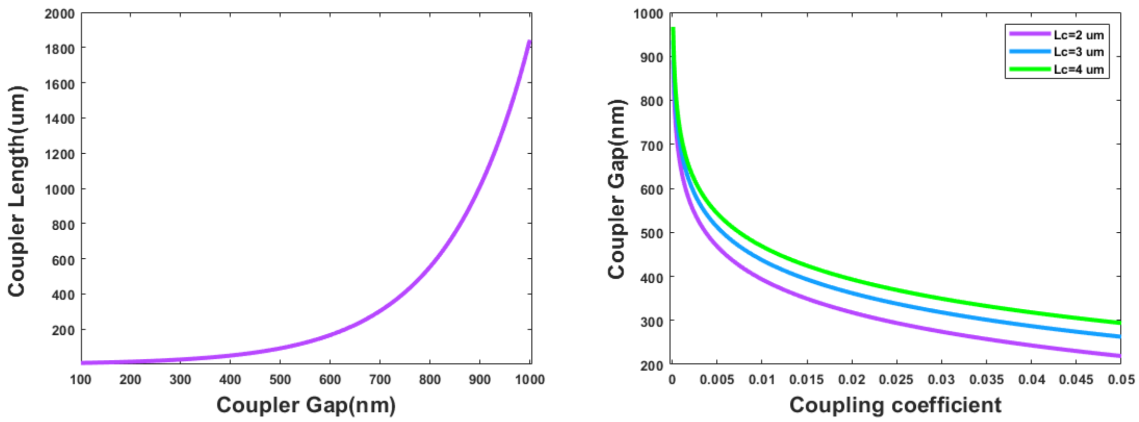

(a) (b)

Figure 2.2: (a) Coupling length as a function of gap. (b) Gap as a function of coupling coefficient for different coupling lengths

2.4 Multimode Couplers

Two waveguides capable of converting power from one mode to another are known as a multimode couplers. Moreover, the waveguides should be as small as possible to achieve high optical light confinement (Ding et al., 2014). Additionally, the ideal coupler is made of waveguides without perturbation, as this causes changes in the mode amplitudes. However, real waveguides can have index perturbations that result from the fabrication process as well as bending of the waveguide (Li et al., 2014).

The coupler can operate in two regimes: weakly coupled and strongly coupled. In the weakly coupled regime, the change in the amplitude of the modes is negligible. However, in the strongly coupled regime, the mode amplitude fluctuates, and all energy can transfer to the other mode.

The efficiency of the mode conversion process is function of the phase-matching between the modes, which can be affected by perturbation and dispersion in the waveguides. To obtain high efficiencies, strong phase-matching is required (Ding et al., 2014).

The coupled power periodically oscillates between the two waveguides. Figure 2.3 depicts a multimode coupler supporting four modes, from TE_0 to TE_3. This coupler illustrates that the energy of the fundamental mode in the first waveguide transfers to the third-order mode in the second waveguide, which means that the power from TE_0 in the first waveguide is strongly coupled to TE_3, and weakly coupled to TE_0, TE_1, and TE_2 in the second waveguide. As explained above, the coupling length and the gap between the waveguides play a prominent role in achieving strong coupling.

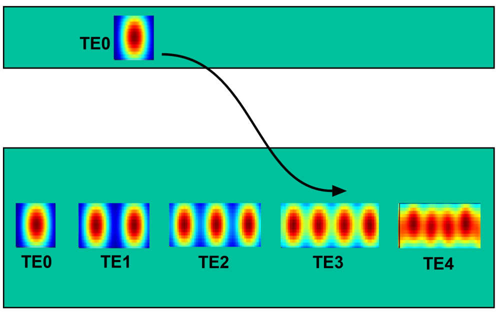

Figure 2.3: Model of a horizontal multimode coupler showing the power transfer between two parallel waveguides from fundamental mode to the TE_3 mode.

2.5 Ring Resonators

A ring resonator consist of a looped waveguide coupled to one or two straight waveguides. When a traveling wave experiences a round trip path length through the looped waveguide equal to an integer number of wavelengths, a resonance occurs at this specific frequency. A simple ring resonator formed using one ring and a directional coupler is known as an All-Pass Filter (APF) and it has one input port and one output port. A ring resonator consisting of one looped waveguide and two directional couplers is known as an Add-Drop Filter (ADF) and it has four ports: one input port, one add port and two output ports called the through port and drop port. Figure 2.4 shows two types of add-drop filters: a conventional Micro-Ring Resonator (MRR) and a Racetrack Resonator (RTR). They operate in a similar fashion, with the only difference being their coupling regions. The RTR has longer coupling regions. The strong coupling between the straight and bent waveguides is complex, as indicated in Fig. 2.4(a), while coupling between the two straight waveguides is readily obtained, as shown in Fig. 2.4(b).

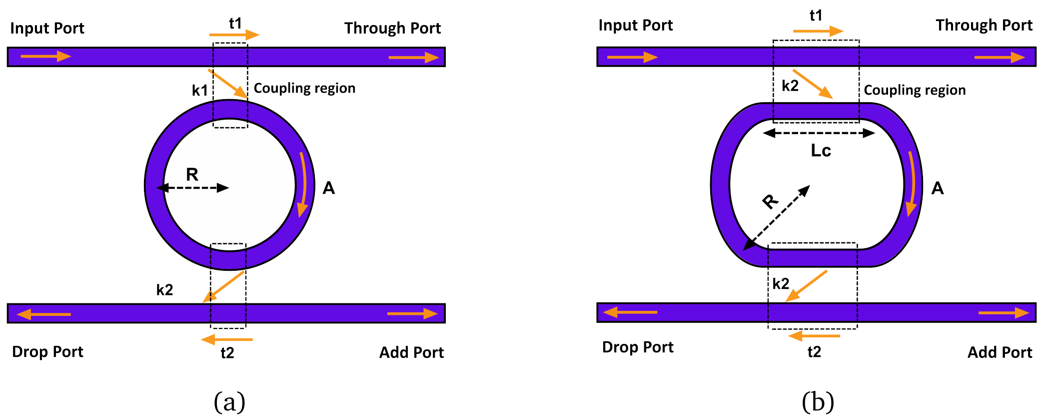

Figure 2.4: Schematic of two types of optical add drop ring filters: (a) a microring and (b) a racetrack resonator.

The total round trip path length of the resonator is defined by:

$$L_{rt} = 2\pi R + 2Lc \tag{2.10}$$

where R and Lc are the radius and coupling length, respectively (the MRR has a coupling length of zero). The distance between the two resonance peaks is given by the FSR (Free Spectral Range) obtained by Eq. 2.11 which relates to the group index (n_g) and the total round-trip path length of the ring. Consequently, depending on the application, it is possible to adjust the FSR by changing the total round-trip path length.

$$FSR = \frac{\lambda_{res}^2}{n_g L_{rt}} \tag{2.11}$$

2.5.1 Coupling Between the Ring and Bus Waveguides

As mentioned in the previous section, the resonance is constructed by injecting a fraction of the incoming field into the ring while it experiences a total round-trip path length corresponding to an integer number of wavelength. The behavior of the ring resonator is function of two coupling coefficients: the self-coupling coefficient (t) and cross-coupling coefficient (k). The self-coupling coefficient is defined as the fraction of the input power (P_{in}) passing through the directional coupler and then reaching the through port. The cross-coupling coefficient is defined as the fraction of input power that transfers between the bus waveguide and the ring, in a section called the coupling region, which is shown in Fig. 2.4. In other words, the power couples from the bus waveguide to the curved waveguide; afterward, the optical power can exit through the drop port. For a symmetric ring resonator, it is assumed that $t_1 = t_2$ and $k_1 = k_2$ requiring the same gap at the top and bottom. Furthermore, it is assumed that the couplers are lossless, hence $t^2+k^2 = 1$. However, in asymmetric ring resonators, $t_1 \neq t_2$ and $k_1 \neq k_2$. An asymmetric ring includes a ring with two asymmetric bus waveguides (with different width). Using buses of different widths requires different gaps, which is more challenging to design compared to symmetric rings.

The optical power transfer depends on the round-trip phase (ϕ), and power attenuation (A), which were calculated by Bogaerts and Chrostowski (2018):

$$A^2 = e^{-\alpha Lrt} \tag{2.12}$$

$$\phi = \beta L_{rt} = 2\pi m \tag{2.13}$$

where α is the propagation loss inside the coupler and β is the propagation constant of the traveling mode through the waveguide, which is determined by:

$$\beta = \frac{2\pi n_{eff}}{\lambda_{res}} \tag{2.14}$$

where n_{eff} is the effective refractive index of the selected mode. In addition, the power coupling between the selected mode can be computed by:

$$P_{coupling} = k^2 \tag{2.15}$$

The ideal ring is lossless, which means that the power attenuation coefficient (loss) is zero ($A^2 = e^{-\alpha Lrt} = e^0 = 1$). Under the condition where the coupled power through the ring is equal to the power attenuation (i.e. losses), the intensity at the drop port is zero; therefore, we have $A = t$ and $A^2 + k^2 = 1$. When the phase shift accumulated inside the ring is an integer of multiple 2π and the power attenuation coefficient is negligible (lossless cavity $A = 1$), the incident light will be in resonance (Heebner et al., 2008). The transmission characteristics of the ring resonator and optical phase shift are shown in Fig. 2.5 as given by Okamoto (2021).

$$\varphi = \pi + \phi + \arctan \frac{t \sin\phi}{A - t\cos\phi} + \arctan \frac{tA\sin\phi}{1 - tA\cos\phi} \tag{2.16}$$

Figure 2.5(a) represents the ideal transmission response of a ring resonator where all the incoming power at the resonant wavelength is coupled to the drop port, with no power going to through port. The effective phase delay for the lossless ring resonator ($A = 1$) is shown in Fig. 2.5(b). When the cross-coupling coefficient (k) is strong enough, t=A; this condition is called the critical coupling condition. However, if $t > A$ or $t < A$, then the ring is in the under coupling or over coupling conditions, respectively. Consequently, to achieve a strong coupled power in the ring resulting in a high transmission, we must create a ring with the lowest loss possible at the resonance. In addition, the resonant wavelength is function of the round-trip path length and effective index of traveling mode, which can be calculated with:

$$\lambda_{res} = \frac{n_{eff} L_{rt}}{m} \quad , \quad m = 1, 2, ... \tag{2.17}$$

where m is the order of the resonances. To align the resonance at a specific wavelength, changing the total round-trip path length is required.

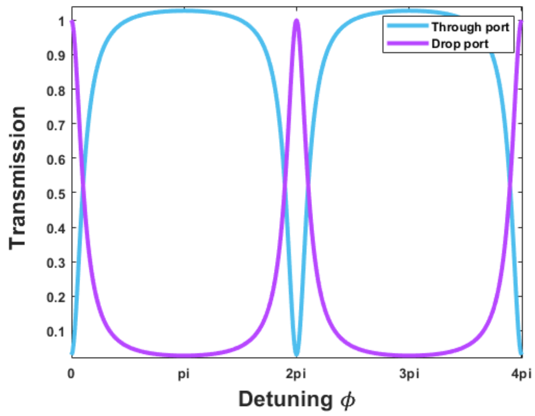

(a)

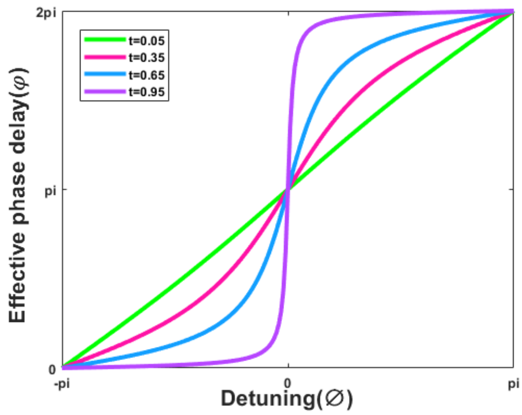

(b)

Figure 2.5: (a) Simulated transmission spectrum of the ring resonator as a function of phase detuning while operating in the critical coupling condition. (b) Effective phase delay for different coupling coefficients.

2.5.2 Bandwidth

The Full Width at Half Maximum (FWHM) or 3-dB bandwidth is dependent on the loss inside the ring. An ideal ring produces a narrow FWHM since the losses are low at the resonant wavelength. The analytic equation to calculate the FWHM of add-drop filter ring resonators is:

$$FWHM = \frac{(1 - t_1 t_2 A)\lambda_{res}^2}{\pi ng L_{rt}(\sqrt{t_1 t_2 A})} \tag{2.18}$$

2.5.3 Finesse and Quality Factor

Two other parameters related to the FWHM are the finesse and the Quality factor (Q factor). The finesse characterizes the spectral shape of the response of the ring and can be calculated with Eq. 2.19. The finesse represents the sharpness of the resonance relative to the FSR. In contrast, the Q factor represents the sharpness of resonance relative to the resonant wavelength, as shown by Eq. 2.20. Accordingly, the Q factor indicates the relationship between the energy traveling inside the ring and the power lost during each round trip around the ring (Heebner et al., 2008). To increase the Q factor, the loss should be reduced.

$$Finesse = \frac{\pi\sqrt{t_1 t_2 A}}{1 - t_1 t_2 A} \approx \frac{FSR}{FWHM} \tag{2.19}$$

$$Qfactor = \frac{\pi ng L_{rt}\sqrt{t_1 t_2 A}}{\lambda_{res}(1 - t_1 t_2 A)} \approx \frac{\lambda_{res}}{FWHM} \quad (2.20)$$

2.5.4 Crosstalk

In this study, we consider the following three concepts related to crosstalk: crosstalk suppression, adjacent channel crosstalk, and inter-modal crosstalk.

Crosstalk suppression relates to the difference between the drop and through port responses at the same resonant wavelength, which is mainly function of the coupling coefficient (Mansoor et al., 2015). When the coupling coefficient satisfies the critical coupling condition a high level of crosstalk suppression can be achieved, as expected. Nevertheless, crosstalk suppression decreases as the loss inside the ring increases. Ideally, the crosstalk suppression should exceed a minimum of 20 dB in WDM communication networks.

Optical adjacent channel crosstalk is measured between the two separate channels by calculating the difference between the through port intensity of the first channel and the drop port intensity of the second channel (Mansoor et al., 2014). This crosstalk is influenced by the channel spacing; wider channel spacing minimizes the crosstalk between the two channels (Bahadori et al., 2016). The wavelength difference between the channels at resonance is known as the channel spacing.

Crosstalk suppression and adjacent channel crosstalk are function of the relative intensity of different signals propagation in the same mode (typically the fundamental mode), whereas optical inter-modal crosstalk represents the relative intensity between the different modes at the same resonant wavelength. Furthermore, inter-modal crosstalk is critical in MDM communication networks since each mode operates as an individual channel.

2.6 Conclusion

This chapter reviewed the theory of modes propagating through waveguides. We gave an overview of the two elements widely used in multiplexers: directional couplers and ring resonator. A brief theoretical discussion of the add-drop filter properties was presented. We summarized the concepts required to explain the ring resonator behavior. In addition, the parameters that have significant impacts on the optical characteristics of the ring resonator have been discussed.

Chapter 3

Literature Review

3.1 Optical Multiplexing

Optical Multiplexing is a key component in WDM and MDM optical links on both the transmitter and receiver sides. On the transmitter side, multiplexing combines optical signals whereas on the receiver side, it splits or filters the modulated signals and is therefore referred to as demultiplexing (Wang, 2016). A (de)multiplexer performance can be characterized by several features such as its insertion loss, crosstalk, group delay, and 3-dB bandwidth. The crosstalk is caused by the superposition of desirable and undesirable optical signals leading to an increase in the Bit Error Rate (BER). As a result, optical multiplexing with low crosstalk is essential (Mansoor, 2015).

Recently, many promising implementations of optical multiplexers have been demonstrated using micro-ring or racetrack resonators, Asymmetric Directional Couplers (ADCs), Mach–Zehnder Interferometers (MZIs), Y-junctions, and Array Waveguide Gratings (AWGs). The remainder of this chapter will review the recent progress on silicon photonic devices for WDM and MDM.

3.1.1 WDM Multiplexing

This section describes CWDM and DWDM (de)multiplexing based on MZI and micro-rings. A four-channel CWDM (de)multiplexer based on two-stage cascaded MZIs was fabricated by Yen and Hung (2020). This configuration can provide wide FSRs of 40 nm or 80 nm. The four channels have a 3-dB bandwidth larger than 10 nm.

The fabricated CWDM (De)MUXs consist of 10 MZIs and directional couplers with five different coupling coefficients at 1550 nm: 0.5, 0.3, 0.23, 0.17, and 0.05. The simulated 4-channel CWDM (De)MUX suffers from a high insertion loss of 2.2 dB $\sim$ 7.3 dB and channel crosstalk of -7 dB $\sim$ -21 dB, whereas another version with fabrication-tolerant MZI design has an insertion loss of 1.6 dB $\sim$ 3.7 dB and channel crosstalk of -16 dB $\sim$ -28.6 dB.

Another proposed configuration for WDM optical multiplexing based on the combination of MZI and MRR was demonstrated by Zhang et al. (2015). Four asymmetric MZI were used to modulate signals at different wavelengths and implementing four rings to couple the modulated signals to a common bus. As it was a DWDM, a channel spacing of 2.4 nm was considered. This structure had a 21.5 dB fiber-to-fiber insertion loss and a 23 dB on-off extinction ratio.

Tan et al. (2014) designed a 1×4 WDM based on micro-rings, including coupled vertical gratings to mitigate the ripple in the transmission spectrum. The four channels were centered at 1554 nm, 1560.5 nm, 1567 nm, and 1573.5 nm. The 6.5 nm of channel spacing was chosen to decrease the footprint and complexity of the wavelength selector. This WDM had 1 dB of insertion loss, a 3-dB bandwidth of 0.5 nm, and 16 dB crosstalk suppression.

Uddin et al. (2021) presented a four-channel DWDM based on micro-rings to investigate the impact on channel spacing of the ring radius and studied three different radii of 1 μm, 5 μm, and 10 μm. The effect of the radius on FSR and Q factor was studied to demonstrate that small FSRs limit the available bandwidth. In other words, with wider FSR, WDM applications are capable of supporting a higher number of channels. In this study, the reference rings had FSRs of 83.18 nm, 17.38 nm, and 8.63 nm. Additionally, a 0.02 coupling coefficient was reported.

3.1.2 MDM Multiplexing

This section introduces several studies on MDM (de)multiplexing. A three-channel MDM (de)multiplexer based on identical single-mode racetrack resonators was fabricated by Luo et al. (2014), with a common bus waveguide supporting multiple TE modes: TE_0, TE_1, and TE_2. Three rings with a 10 μm radius and 5 μm coupling length were fed by the same transmitter. The fabricated device included both the multiplexer and demultiplexer sides. In this work, the authors made efforts to reduce inter-modal crosstalk. To decrease the crosstalk below -30 dB, a larger coupling length and coupling gap were suggested. The crosstalk between TE_0 and TE_2 improved to -16 dB at the output of the multiplexer.

Zheng et al. (2018) followed the same design as Luo et al. (2014) but used the modes TE_1, TE_2, and TE_3 at λ= 1540 nm as the first, second, and third output ports, respectively. In this study, the average crosstalk of the device was less than -12 dB.

A four-channel MDM multiplexer was fabricated by Jia et al. (2019), but the demultiplexer side was not studied. The four cascaded asymmetric racetrack rings supported modes TE_0 to TE_3 and had a 10 μm radius, 2 μm coupling length, and a coupling coefficient of 0.4. This multiplexer is designed to be fed by cascaded 1×2 MMI power splitters over the wavelength range from 1525 nm to 1565 nm. In this study, a FSR of 9.1 nm was reported. Furthermore, the insertion loss and extinction ratio of the device were less than 1.9 dB and more than 19.6 dB, respectively. The fabrication process slightly shifted the resonance wavelength of the four-mode channels.

Table 3.1 shows the optical specifications of the three works described above relative to the dominant modes at each output port.

Table 3.1: Optical specifications of MDM multiplexing.

Mode Number (Luo et al., 2014)	Insertion Loss (dB)	Crosstalk (dB)		
TE_0 at output port1	13	-22		
TE_1 at output port2	19	-18		
TE_2 at output port3	26	-12		
Mode Number (Zheng et al., 2018)	Insertion Loss (dB)	Crosstalk (dB)		
Port1 supports TE_1	5	-20		
Port2 supports TE_2	14.5	-12		
Port3 supports TE_3	11.5	-15		
Mode Number (Jia et al., 2019)	Insertion Loss (dB)	Crosstalk (dB)	Drop port ER (dB)	Q factor
TE_0 at output port1	1.3	-13.7	20.6	2,153
TE_1 at output port2	1.5	-11.5	20.2	2,039
TE_2 at output port3	1.5	-11.7	20.2	2,039
TE_3 at output port4	1.9	-10.8	19.6	2,089

A four-mode division de(multiplexer) based on three tapered asymmetrical directional couplers with four input/output ports was fabricated by Qiu et al. (2017). This device was designed with a tapered structure since it is more fabrication tolerant and has a wide working bandwidth in comparison to conventional asymmetrical directional couplers. In this design, the common bus waveguide supports modes TE_0 to TE_3. The average insertion loss for the modes TE_0, TE_1, TE_2, and TE_3 is 1.3 dB, 2.6 dB, 4.8 dB, and 5 dB, respectively. At the same time, the average crosstalk of the four channels over a wide wavelength range of 70 nm was reported as less than -18 dB.

Nath et al. (2020) demonstrated a five-mode division multiplexer, including two coupling sections consisting of two asymmetric directional couplers. In this design, the number of guided modes is controlled by the number of coupling regions, which means that in order to support more modes, more coupling regions are required. The proposed configuration guides five modes from TE_0 to TE_4 for which the device has a maximum insertion loss of 0.24 dB and crosstalk of less than -33 dB at 1550 nm. This work introduced a compact mode division (de)multiplexer with a total length of 38.89 μm.

3.1.3 Thermal Behavior of Rings

This section addresses the thermal sensitivity of the ring resonators. Bogaerts et al. (2012) focused on the optical specifications of silicon micro-ring resonator. One prominent study showed how the resonant wavelength was affected by temperature. They investigated the response of a 2^{nd} order ring filter as a function of temperature. The temperature was varied from 25 $°C$ to 60 $°C$ and the resonant wavelength shifted by 0.102 $nm/°C$.

Rouger et al. (2010) modeled a racetrack resonator to demonstrate how it is affected by temperature. This racetrack was simulated with a 10 μm radius and a 5 μm coupling length. In this work, the resonant wavelength shift reported was 0.0806 nm/K.

Liu et al. (2019) studied a PV (process variations)-tolerant thermal sensor that included a multi-wavelength source feeding four micro-rings add-drop filters. The silicon micro-rings were designed with a 5 μm radius and a 100 nm gap. In that study, shifts in wavelength due to variations in temperature were evaluated over the range from 300 K to 380 K. A 0.06 nm/K wavelength shift was reported.

Li et al. (2018) demonstrated orbital angular momentum multiplexing based on a multimodal micro-ring resonator, which can be used in MDM communications. The micro-ring has a width of 0.95 μm and a radius of 9.95 μm. The temperature sensitivity reported was 0.078 nm/K and 0.076 nm/K for the TE_0 and TE_1 mode, respectively.

In this dissertation, we simulated a silicon four-channel ring-based WDM and MDM multiplexer. The temperature was tuned from 25 $°C$ to 75 $°C$. The two devices showed a similar resonant wavelength shift of 0.078 $nm/°C$.

Therefore, numerous reports available in the literature show that controlling the operating temperature is critical to the performance of devices built using micro-ring resonators. However, there are very few publications addressing the impact that temperature variations can have on MDM devices and none that compare the performance of WDM vs MDM as a function of temperature.

3.2 Conclusion

This chapter surveyed recently proposed designs for WDM and MDM devices. As illustrated, most WDM are simulated and fabricated based on MZIs or micro-rings. However, MDM have been designed using racetrack resonators or tapered directional couplers.

In particular, silicon ring resonators are a promising approach. Ring-based WDM devices have a narrow bandwidth selectivity and a small footprint (De Cea et al., 2019). Furthermore, ring resonators are suitable for both on-chip WDM and MDM since asymmetric ring resonators with directional couplers with different widths can be used.

However, silicon ring resonators are highly sensitive to environmental changes (e.g., temperature) and dimension variations (Wu et al., 2016). One possible solution proposed to make the waveguide less sensitive is using the less confined transverse magnetic (TM) polarization (De Heyn et al., 2013).

Following this review of the literature, it is clear that micro-ring resonators are suitable to implement both types of multiplexing techniques that are the subject of this study. Nevertheless, as demonstrated in the literature, the response of micro-ring resonators can shift significantly as a function of temperature. Moreover, there are very few investigations about the impact of variations in temperature on MDM devices. Therefore, this work attempts to fill that gap by performing a comparative study between WDM and MDM multiplexers. Ring-based multiplexers will enable to compare the effect of temperature on devices with similar architecture but the channels are either different frequencies or special modes.

Chapter 4

WDM Optical Demultiplexing

4.1 WDM Design

This chapter presents a four-channel wavelength demultiplexer based on silicon micro-rings where the channels are aligned on the ITU 200 GHz grid. Figure 4.1 shows a schematic of the WDM demultiplexer. The four rings are coupled to a bus waveguide connected to a source that emits signal at four different wavelengths. Each ring is designed to resonate at the wavelength of a specific channel, which is then transferred to the drop waveguide at the bottom of the ring. Since each ring is connected to a different drop waveguide, the device effectively separates each channel that could then be converter to the electrical domain with a photodetector, for instance.

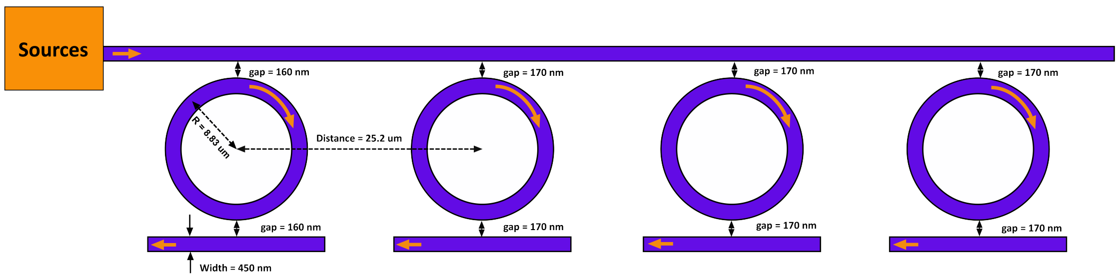

Figure 4.1: Schematic of the four-channel cascaded symmetric ring-based WDM demultiplexer.

In the design shown above, the silicon core is surrounded by a silicon dioxide bottom cladding and an air top cladding. All micro-rings are made of waveguides that are 450 nm wide and 220 nm thick. The proposed WDM demultiplexer is formed by four cascaded symmetric micro-rings supporting the TE fundamental mode having an effective index of 2.27 at λ =1550 nm. The micro-rings have a bending radius of approximately 8.83 μm and the difference in radius between the rings is only 17.3 nm. The rings are spaced 25.2 μm apart, and the center-to-center distance of the neighboring rings was considered when defining the Perfect Matched Layers (PML) boundaries on the x-axis of the simulations. PML boundaries must be precisely chosen to obtain consistent simulation results. The center-to-center distance needed to minimize coupling between the rings can be calculated with Eq. 4.1 proposed in Huang et al. (2009). In the device described here, the four micro-rings have approximately the same FSR since the 8.83 μm radius results in a FSR of 9.86 nm.

$$D = \pi R + \frac{\lambda_{res}}{4n_{eff}} \tag{4.1}$$

One critical parameter that requires attention to achieve the critical coupling condition is the size of the gap between the ring and the bus waveguide. The optimum gap is the one for which the power at the resonant wavelength is high at the drop port and close to zero at the through port. However, it is impossible to get an absolute value of zero in real life, but minimizing the power coupled at the through port maximizes the extinction ratio (ER), which will be discussed in further details in the following section. In the final design, the optimum gap is 160 nm and 170 nm for the first channel and for the other three channels, respectively. In this approach, the optimum gaps were obtained for the first channel at λ =1550.18 nm, the second channel at λ =1551.73 nm, the third channel at λ =1553.38 nm, and the fourth channel at λ =1554.94 nm.

Studying the critical coupling condition permits finding the optimum gap. In this work, two half micro-rings were modeled with ANSYS Lumerical FDTD solver to calculate the coupling coefficient in both coupling regions. This structure enables separate quantification of the top and bottom coupling coefficient (k_1 and k_2). In symmetric coupling sections, considering that the guided optical modes at both output ports are similar, k_1 and k_2 should be approximately the same. Figure 4.2 depicts the coupling coefficient as a function of wavelength for the first channel, showing that k_1=1.62 % and k_2 =1.69 % at λ =1550.18 nm.

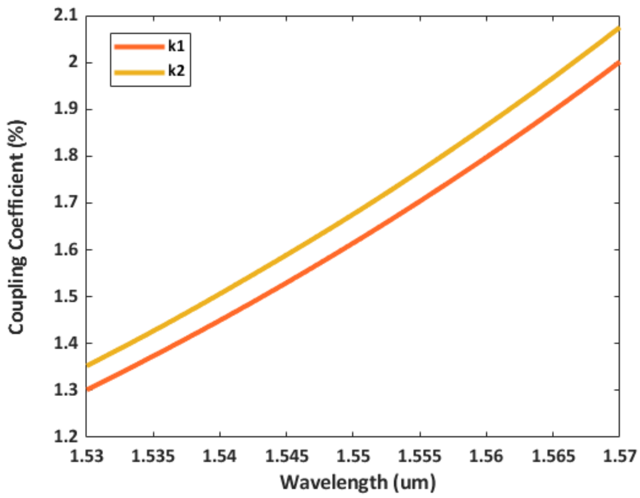

Figure 4.2: Simulated coupling coefficient as a function of wavelength for the 1^{st} channel of the WDM demultiplexer.

4.2 WDM Simulated Responses

This section provides a detailed analysis of the proposed WDM optical properties. The prominent features that significantly affect micro-ring performance were investigated and analyzed. The frequency response of each whole micro-ring was separately obtained at room temperature (25 $^\circ C$) from the ANSIS Lumerical MODE VarFDTD solver; afterward, their S-parameters were directly exported to INTERCONNECT. It is also possible to model a ring-based WDM approach using the VarFDTD solver, which makes the simulation process longer by a couple of days.

4.2.1 WDM Optical Spectrum

In designing this WDM we aimed to maximize the transmission intensity by optimizing the coupling. Figure 4.3 illustrates the spectral transmission of the third channel. As depicted by the simulation response, a transmission with a steep band-edge and low losses is achieved. Figure 4.3 also demonstrates the three coupling conditions representing the critical coupling condition at λ =1553.38 nm and under-coupling and over-coupling conditions at the adjacent resonances. The transmission responses relative to the four-channel WDM are listed in Table 4.1. The minimum drop port and maximum through port normalized transmission intensity achieved are 0.94 and 1.5×10^{-3}, respectively, for the second channel.

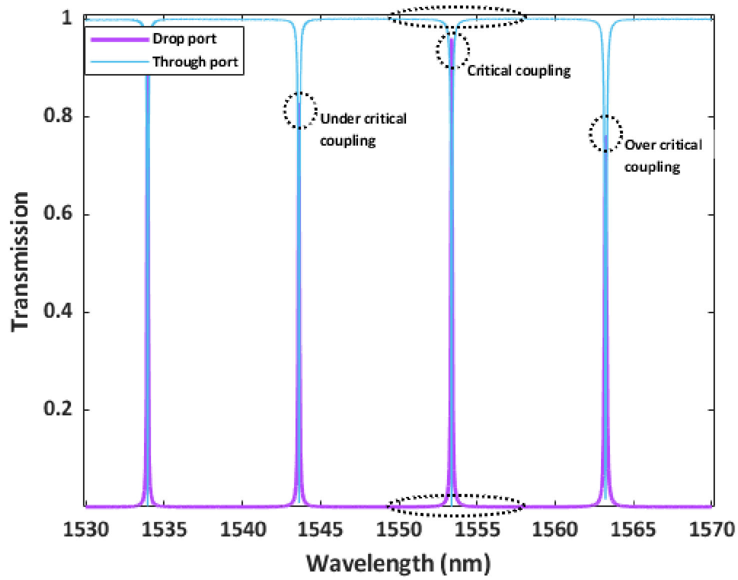

Figure 4.3: Simulated transmission and drop port spectra for the 3^{rd} channel of the WDM demultiplexer obtained with the VarFDTD solver.

Table 4.1: Spectral Characteristics Table: Transmission and extinction ratio of the four-channel WDM demultiplexer.

Channel Number	Drop Port Transmission	Through Port Transmission	Drop Port ER (dB)	Through Port ER (dB)
CH1 at 1550.18 nm	0.99	8.08×10^{-5}	35.93	40.8
CH2 at 1551.73 nm	0.94	1.5×10^{-3}	37.43	27.9
CH3 at 1553.38 nm	0.96	4.6×10^{-4}	37.54	33.04
CH4 at 1554.94 nm	0.96	7.4×10^{-4}	37.3	31.1

Achieving a high transmission intensity also improves the ER. In the case of a ring resonator, two different ERs are considered: the through port extinction ratio and drop port extinction ratio. Figure 4.4 shows the drop and through port ER for the first channel of WDM. As can be seen, the through port ER is 40.8 dB and 43.05 dB at λ =1550.18 nm and λ =1560.04 nm, respectively. Furthermore, the normalized transmission at the drop port is 0.99 and 0.98 at λ =1550.18 nm and λ =1560.04 nm, respectively, resulting in a maximum drop port ER of 35.93 dB. Further information regarding the transmission and ER of the four-channel WDM is listed in Table 4.1.

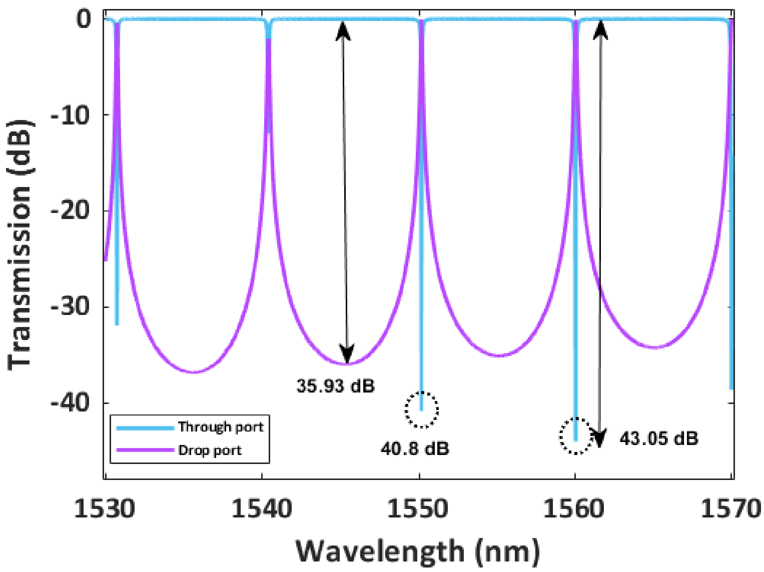

Figure 4.4: Simulated transmission and drop port spectra of the 1^{st} channel of the WDM demultiplexer obtained through S-parameters uploaded in INTERCONNECT.

Figure 4.5 presents the simulated transmission spectra for the four-channel of the ring- based WDM demultiplexer showing that the channel spacing is 1.6 nm. As shown, the maximum and minimum normalized transmission are 0.99 at λ =1550.18 nm and 0.94 at λ =1551.73 nm, respectively. These spectra further demonstrate how a WDM works, showing how each channel corresponds to a specific wavelength. For instance, at λ =1550.18 nm, the power in the last three channels is very low. Likewise, the same behavior is seen for the other channels at the neighboring resonances. Also note that no significant interference was obtained between the channels.

To accurately model the high ER achieved in the first channel, its transmission spectrum was calculated with high precision by increasing the grid resolution of the simulation. This did not affect the intensity at the drop port, which remained the same as before at 0.99 at λ =1550.18 nm. However, the through port transmission decreased to 1.21×10^{-5}, and the effect of the reduction in the power at the through port was to enhance the through port ER to 48.25 dB, as illustrated in Fig. 4.6.

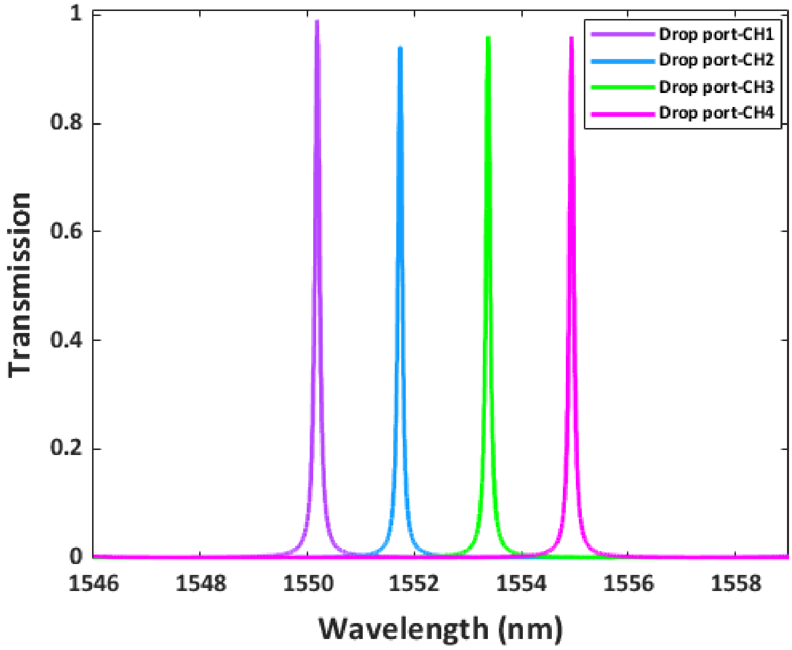

(a)

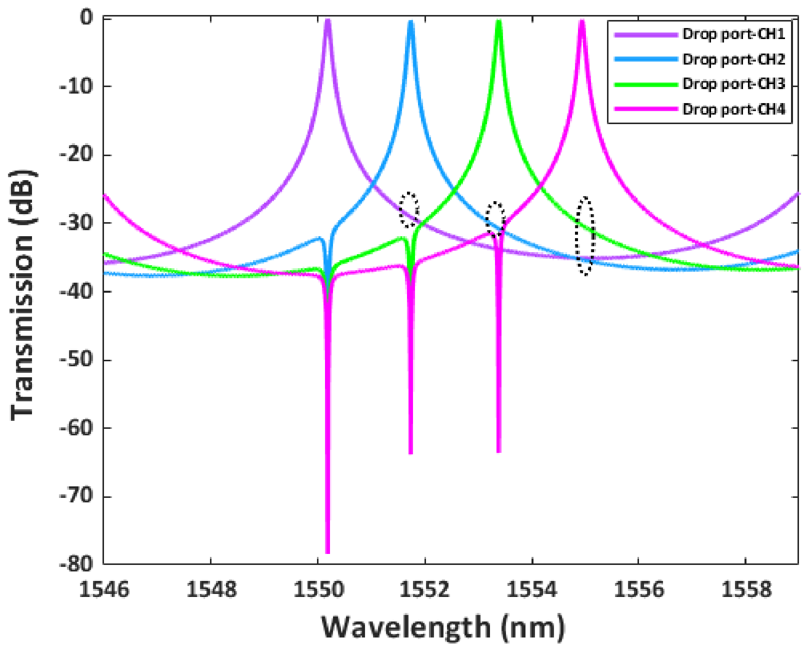

(b)

Figure 4.5: Transmission spectra of the four-channel cascaded symmetric ring-based WDM demultiplexer in (a) linear normalized scale and (b) in dB.

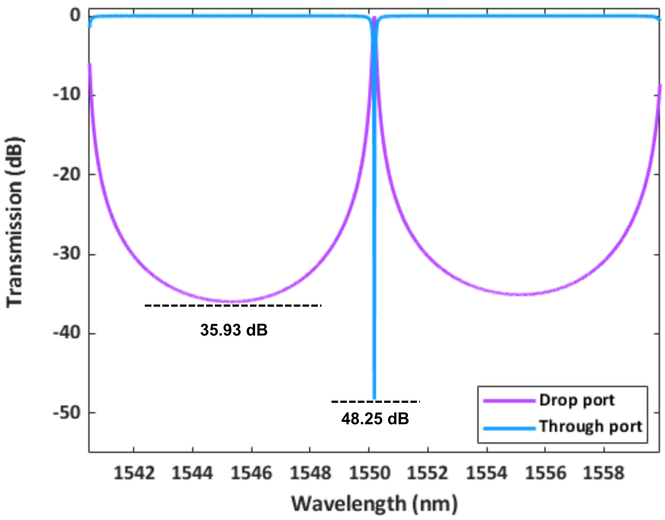

Figure 4.6: Transmission spectrum of the 1^{st} channel obtained with a finer FDTD simulation grid.

4.2.2 Optical Losses

Loss is an important phenomenon affecting the performance of rings. Two types of losses must be considered: Insertion Loss (IL) and Return Loss (RL). Accordingly, a portion of the remaining input power that could not be coupled to the drop port will appear as an insertion loss. Consequently, the insertion loss decreases as the transmission increases at the drop port. Figure 4.7(a) shows the transmission spectrum of the first channel in which the transmission is modified to 0.99 at λ = 1550.18 nm; therefore, 0.01 of the input power appears as a loss, namely insertion loss.

On the other hand, the return loss is the portion of the input power reflected back towards the input. Therefore, it should be maximized as much as possible. Figure 4.7(b) illustrates the return loss behavior as a function of the wavelength. The insertion loss and return loss of the four-channel WDM demultiplexer are detailed in Table 4.2. In the worst case, the maximum insertion loss and the minimum return loss are 0.26 dB and 14.26 dB at λ = 1551.73 nm. The average simulated insertion loss and return loss for the WDM demultiplexing are 0.16 dB and 17.80 dB, respectively.

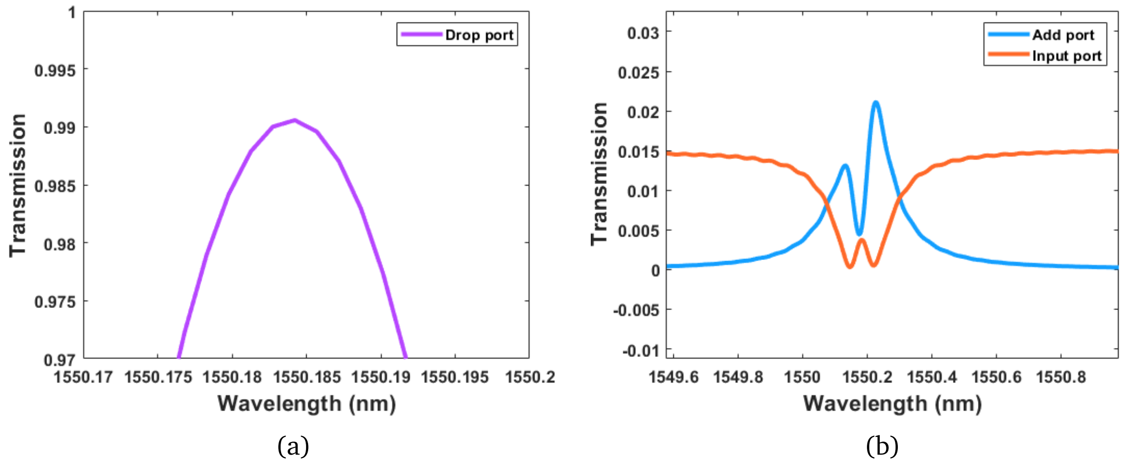

Figure 4.7: Zoom-in view of the simulated transmission spectra of the 1^{st} channel (a) at the drop port and (b) at the input and add ports.

Table 4.2: Simulated loss features for the four-channel WDM demultiplexing.

Channel Number	Insertion Loss (dB)	Return Loss (dB)
CH1 at 1550.18 nm	0.047	24.28
CH2 at 1551.73 nm	0.26	14.26
CH3 at 1553.38 nm	0.17	16.92
CH4 at 1554.94 nm	0.17	15.74

4.2.3 Spectral Characteristics

Extensive optimization of the FWHM bandwidth was carried out for the proposed WDM. In principle, a low-loss ring gives rise to a narrow FWHM. Herein, the entire bandwidth over the level of 3 dB for the four channels is equivalent to 0.09 nm. Their relevant finesse and Q factor characteristics were calculated with Eq. 2.19 and 2.20 and detailed in Table 4.3, showing slight changes in Q factor and finesse resulting from the slight changes in total round trip path length. Meanwhile, the average simulated finesse and Q factor for the WDM demultiplexer are 109.41 and 17,250.25, respectively.

Table 4.3: Simulated finesse and Q factor feature for the four-channel WDM demultiplexer.

Channel Number	Finesse	Q factor
CH1 at 1550.18 nm	109.55	17,224
CH2 at 1551.73 nm	109.55	17,241
CH3 at 1553.38 nm	109.22	17,259
CH4 at 1554.94 nm	109.33	17,277

4.2.4 Crossstalk

As illustrated in the previous sections, a low-loss WDM approach with almost no interference between the channels was achieved. The consequence of this is that very low crosstalk between the WDM channels is present, as shown in Fig. 4.5 and Table 4.2. Figure 4.8(a) shows that the maximum crosstalk obtained is -28.69 dB in the WDM between the first two channels at λ=1551.73 nm. Furthermore, the minimum crosstalk is -35.24 dB between the second and fourth channels. This is because the crosstalk decreases as the channel spacing increases. Moreover, the average crosstalk for the proposed WDM is -32.19 dB. Further details are listed in Table 4.4.

The crosstalk suppression bandwidth of the first channel is presented in Fig. 4.8(b). As shown, this is computed over the wavelength range for which the level of crosstalk is below -20 dB. The four channels benefit from a similar crosstalk suppression bandwidth of 0.01 nm at their resonant wavelengths.

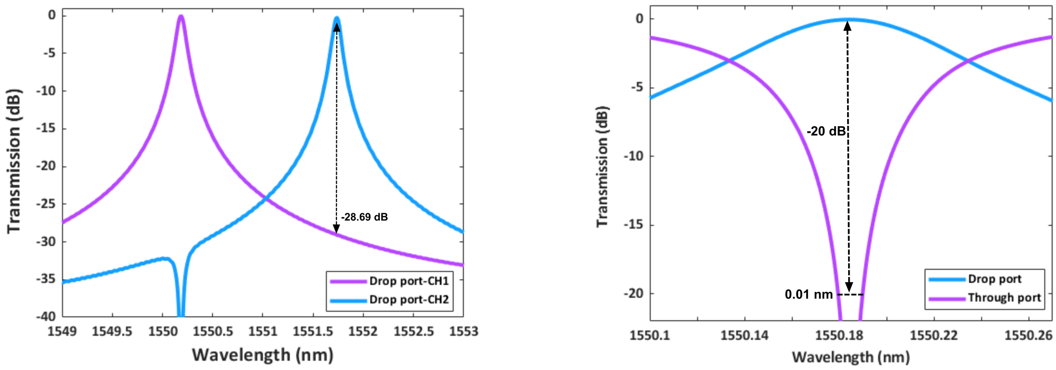

(a) (b)

Figure 4.8: Zoom-in view of the simulated crosstalk in the WDM demultiplexer showing (a) the adjacent channel crosstalk between the 1^{st} and 2^{nd} channels and (b) the crosstalk suppression in the 1^{st} channel as a function of wavelength.

Table 4.4: Simulated adjacent channel crosstalk characteristic between the four channels of the WDM demultiplexer.

Channel Number	CH1 (dB)	CH2 (dB)	CH3 (dB)
CH2 at 1551.73 nm	-28.69	—	—
CH3 at 1553.38 nm	-33.57	-30.56	—
CH4 at 1554.94 nm	-34.90	-35.24	-30.18

4.3 Conclusion

This chapter presented the design and simulation of a four-channel WDM based on silicon micro-rings with a 200 GHz channel spacing. This approach was modeled with an VarFDTD solver and the INTERCONNECT software at room temperature. Designing to reach the critical coupling condition permitted to achieve good optical specifications such as a high ER, low insertion loss, and low crosstalk. This device provides a narrow 3-dB bandwidth and high Q factor for all channels.

Chapter 5

MDM Optical Multiplexing

5.1 MDM Design

This chapter presents the design of a four-channel ring-based mode-division multiplexer. MDM is an emerging technology in optical systems that can be challenging to implement because it requires selectivity between higher-order modes, which is difficult to obtain. In this design, the first task was to modify one of the directional coupler of the micro-rings in order to perform mode conversion. This requires an asymmetric directional coupler. Consequently, a racetrack configuration was used to achieve enough coupling between the resonator and the multimode bus waveguide. The proposed MDM is made of a series of four cascaded identical racetrack resonators that support the TE fundamental mode. A single source could be used to simultaneously launch light in the four input ports with a splitter. Furthermore, the drop bus waveguides of each resonator are linked by 10 μm-long linear tapered waveguides to form a single bus waveguide.

Figure 5.1 shows a schematic of the four-channel MDM multiplexer comprising four identical racetrack resonators, in which the center-to-center distance between the adjacent racetracks is 46 μm. The MDM configuration operates as follows: the first ring from the right couples to the TE_0 mode, the second converts the TE_0 to TE_1 mode, the third converts TE_0 to the TE_2 mode, and finally the fourth converts TE_0 to the TE_3 mode. The drop ports of all the rings are connected by adiabatic tapers that ensures that the signals from the previous channels remain in the desired mode. The frequency response of each racetrack resonator was scanned at room temperature using a similar method to the micro-ring used in the WDM demultiplexer.

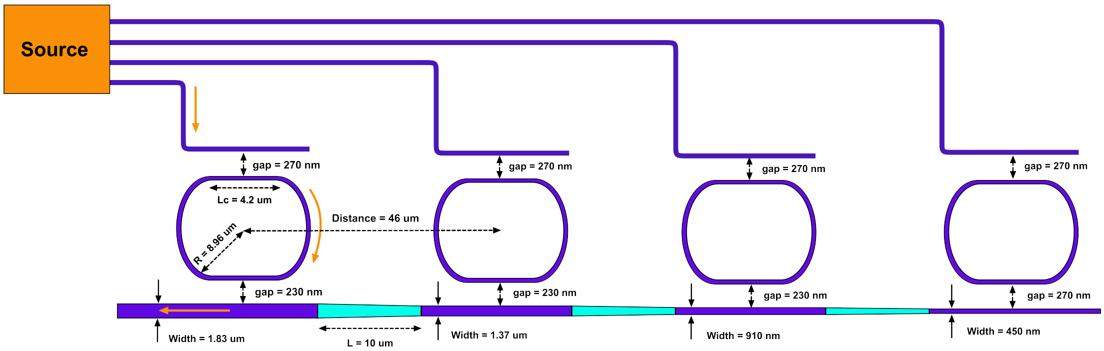

Figure 5.1: Schematic of the four-channel cascaded asymmetric ring-based MDM multiplexer. The optical light coming from a single-mode source is split to feed all the channels simultaneously.

The racetrack resonators have the same silicon waveguide cross-section as the micro-rings used in the WDM approach (450 nm in width and 220 nm in thickness). Each single-mode racetrack resonator was designed to support the TE fundamental mode but they are coupled to different modes of the drop bus waveguide. According to the phase matching condition, the fundamental mode can be coupled to higher order modes in an adjacent multimode waveguide when both modes have identical propagation constant. To achieve this, the multimode waveguide width is adjusted to match the propagation constant of the TE_0 mode of the racetrack resonator with a specific higher-order mode in the multimode waveguide. In this study, the TE_0 coming from the single-mode resonators is coupled with the TE_0, TE_1, TE_2, and TE_3 modes of the drop bus waveguides. Thus, the effective indexes of the TE_0, TE_1, TE_2, and TE_3, which are directly related to their propagation constant, match the effective index of 2.27 of the TE_0 mode in the racetrack at λ=1550 nm. This was done by scanning width of the bus waveguide and calculating the optical modes in two different ways: using a FDE solver and the mode expansion monitor available in the MODE simulation software. The minimum recommended drop bus waveguide widths to match the effective indexes of the resonator mode to the four channels are 450 nm, 910 nm, 1.37 μm, and 1.83 μm, respectively.

In the case of the asymmetric racetrack resonator scheme, a low coupling strength is needed to be able to convert all the power from the fundamental mode propagating in the single-mode racetrack to the higher-order mode in the multimode bus waveguide. Moreover, as little power as possible should be coupled to the other modes. Consequently, studying the coupling regions and coupling coefficient behavior is essential. Due to the asymmetric racetrack scheme, both coupling regions and coupling coefficients must be optimized individually, which is not a straightforward process. To perform this, a study on the impact of the coupling length was accomplished. In this work, all racetrack resonators have a bending radius of 8.96 μm and a coupling length of 4.2 μm, resulting in strong power coupled to the desired mode with a steep response near the resonance and a narrow 3-dB bandwidth. Racetracks with such parameters have a FSR of 8.61 nm.

The gap in the couplers was designed to meet the critical coupling condition. The optimum gap between the input single-mode bus waveguide and single-mode racetrack resonator was found to be 270 nm, whereas the gaps between the single-mode racetrack resonator and the TE_0, TE_1, TE_2, and TE_3 bus waveguides are 270 nm, 230 nm, 230 nm, and 230 nm, respectively.

Figure 5.2 shows the coupling coefficient between the top single-mode bus waveguide and the racetrack resonator (k_1), where the signal remains in the fundamental TE_0 mode, and between the racetrack resonator and the bottom multimode bus waveguide (k_2), where in this example, the TE_0 mode is coupled to the TE_3 mode. This occurs in the leftmost ring in Fig. 5.1. These responses were obtained using a similar technique to that explained in Chapter 4. This design results in k_1= 2.21% and k_2 = 1.10% at λ =1565.66 nm at the last output port. A 1.11% difference between k_1 and k_2 is observed, when the ring is optimized to transfer a maximum of power from the TE_0 to TE_3.

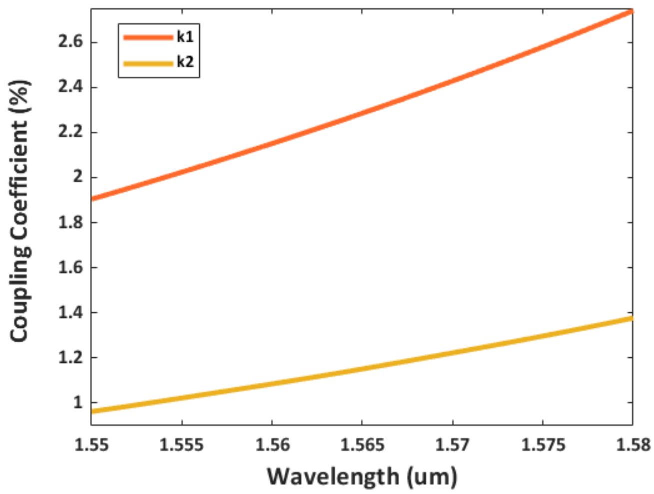

Figure 5.2: Simulated coupling coefficients as a function of wavelength for the last resonator of the MDM multiplexer where the fundamental mode is coupled to the TE_3 mode.

5.2 MDM Simulation Results

This section presents the optical characteristics of the MDM and ends with a brief discussion of the linear tapered waveguide.

5.2.1 MDM Optical Spectrum

Each resonator was simulated separately to demonstrate how the conversion to higher-order modes is performed. A slightly better simulated spectral transmission response was obtained for the fundamental mode channel, which is coupled through the rightmost ring in Fig. 5.1, when λ=1574.23 nm. However, for the higher-order modes, the optimum response was obtained when λ=1565.66 nm as illustrated in Fig. 5.3(a) which shows the TE_2 mode at the output of the third ring. Thus, the study of the MDM focused on this wavelength. Meanwhile, the undesirable modes do not achieve the same level of coupling as the dominant mode. This is illustrated in Fig. 5.3(b), which depicts the spectrum of the TE_2 mode at the output of the fourth ring, which is optimized to couple the TE_3 mode. A considerable difference in coupled power is observable between the drop ports of the third and fourth ring when comparing the spectra shown in Fig. 5.3(a) and (b). The normalized transmitted intensity in the TE_2 mode decreases from 0.92 to 8×10^{-4} at λ=1565.66 nm. More significantly, the low coupled power in the undesired modes is essential to reduce crosstalk between the modes, as will be discussed in the next section.

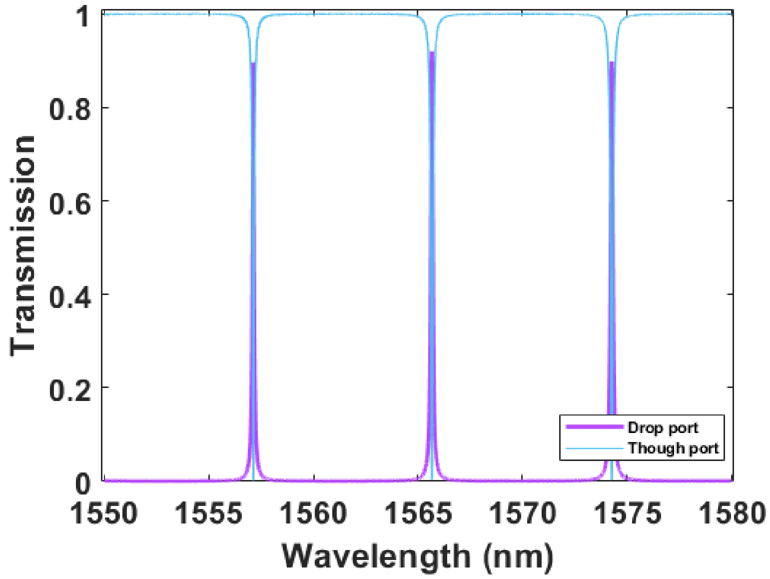

(a)

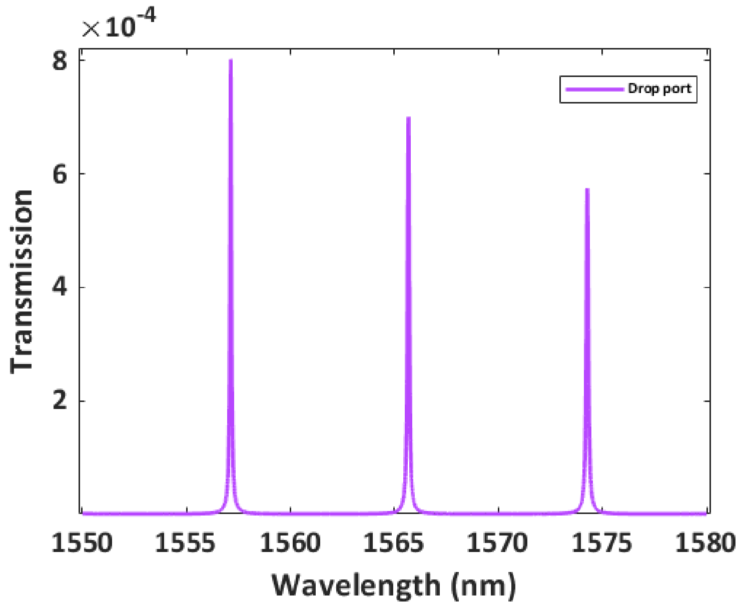

(b)

Figure 5.3: (a) Transmission and drop port spectra of the 3^{rd} resonator in the MDM multiplexer where the fundamental mode coming from the source is converted to the TE_2 mode at the drop port. (b) Spectrum of the TE_2 mode at the drop port of the 4^{th} resonator showing that for this channel very little power is converted into that mode.

The simulated transmission spectra showing the inter-modal crosstalk levels at the four output ports are presented in Figs. 5.4 to 5.7. They demonstrate that each mode operates as a specific channel within the desired wavelength range at each drop bus, which is why MDM can increase the capacity of optical systems. Figure 5.7 shows the transmission spectrum of the four MDM modes with approximately the same coupled power in the TE_1 and TE_2 while maintaining a high difference in coupled power between the TE_3 and the other modes, resulting in low inter-modal crosstalk. The transmission characteristics for the desired modes at the output of the four rings at λ=1565.66 nm are detailed in Table 5.1. The lowest performance is obtained for the TE_3 at the output of the last ring. Its drop and through port normalized transmissions are 0.86 and 3.1×10^{-2}, respectively. Additionally, the maximum normalized drop port transmission, which has a value of 0.97, is obtained for the TE_1 mode at the output of the second ring. Moreover, in this study the minimum through port ER and maximum drop port ER achieved are 14.43 dB and 35.67 dB, respectively, for the TE_3 mode. The maximum through port ER obtained is 30.27 dB for the TE_0 mode. Further details are listed in Table 5.1.

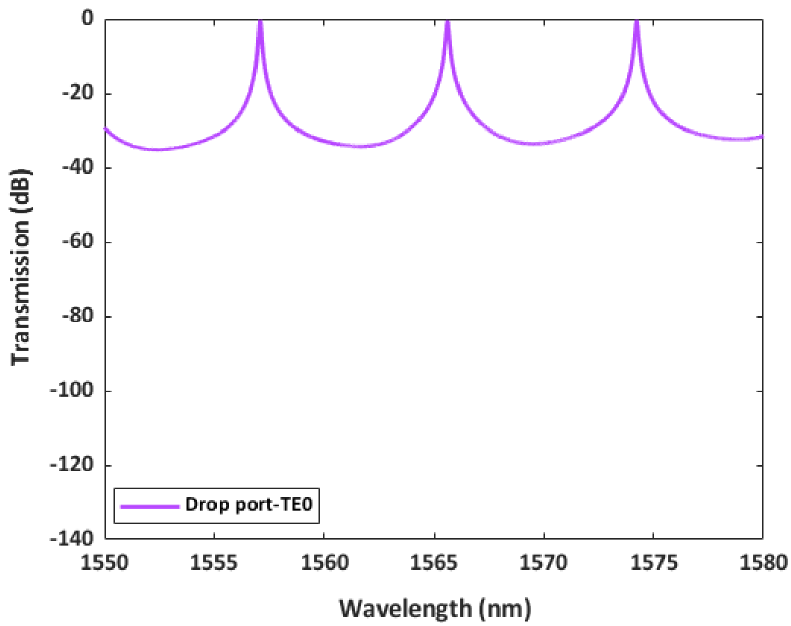

Figure 5.4: Spectrum at the drop port of the 1^{st} resonator where only the TE fundamental mode is present.

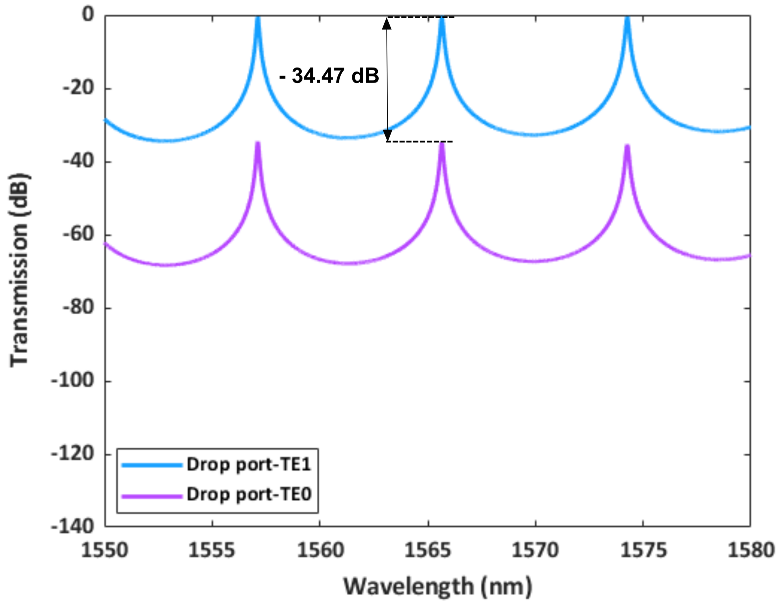

Figure 5.5: Spectrum at the drop port of the 2^{nd} resonator where the input signal is converted to the TE_1 mode. A small fraction of the inside light couples to the fundamental mode at the output.

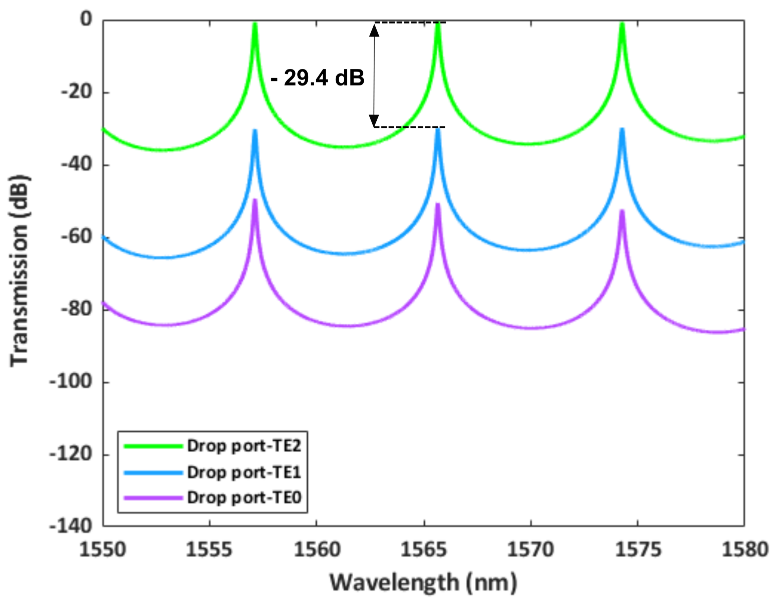

Figure 5.6: Spectrum at the drop port of the 3^{rd} resonator where the input signal is converted to the TE_2 mode showing that there is a little bit of leakage to the TE_0 and TE_1 modes.

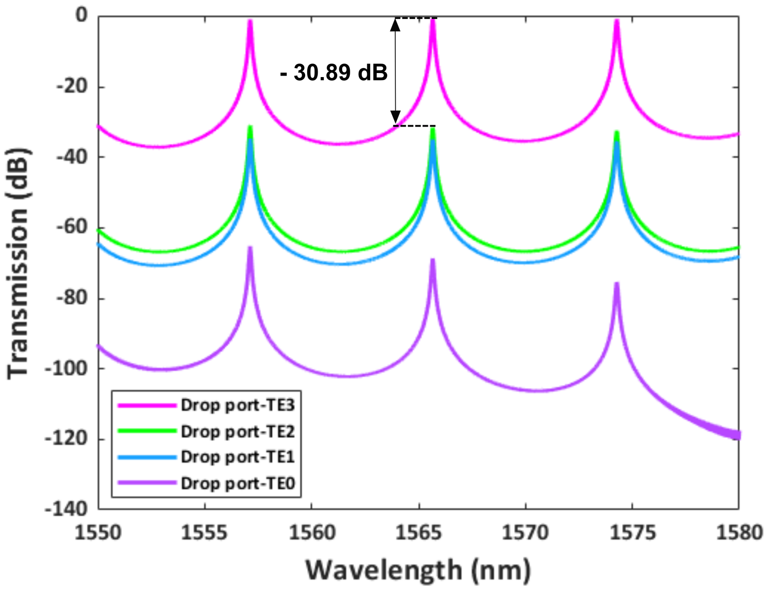

Figure 5.7: Spectrum at the drop port of the 4^{th} resonator where the input signal is converted to the TE_3 mode showing the power leaked into the TE_0, TE_1, and TE_2 modes.

Table 5.1: Spectral Characteristics Table: Transmission and extinction ratio associated with the desired modes at the four output ports at λ=1565.66 nm.

Mode Number	Drop Port Transmission	Through Port Transmission	Drop Port ER (dB)	Through Port ER (dB)
TE_0 at output port1	0.96	8.99×10^{-4}	34.03	30.27
TE_1 at output port2	0.97	8.5×10^{-3}	33.33	20.54
TE_2 at output port3	0.92	3.96×10^{-3}	34.75	23.72
TE_3 at output port4	0.86	3.1×10^{-2}	35.67	14.43

5.2.2 Optical Losses

Insertion loss and return loss in the different mode channels are detailed in Table 5.2. A maximum insertion loss of 0.65 dB and minimum return loss of 20.26 dB are achieved for the TE_3 mode at λ=1565.66 nm. In contrast, the TE_1 mode experiences a low insertion loss of 0.14 dB. In addition, the average simulated insertion loss and return loss for MDM multiplexer are 0.33 dB and 28.23 dB, respectively.

Table 5.2: Simulated loss features at the desired modes traveling through the four output ports of the MDM multiplexing at λ= 1565.66 nm.

Mode Number	Insertion Loss (dB)	Return Loss (dB)
TE_0 at output port1	0.18	51.04
TE_1 at output port2	0.14	21.06
TE_2 at output port3	0.36	20.57
TE_3at output port4	0.65	20.26

5.2.3 Spectral Characteristics

Table 5.3 presents the FWHM, finesse, and Q factor of the four mode channels. The simulated wavelength responses show that the modes have slightly different 3-dB bandwidth. The minimum FWHM is 0.1 nm for the TE_2 and TE_3 modes, which corresponds to a Q factor of 15,656. In addition, the average simulated finesse and Q factor for the MDM multiplexer are 80.55 and 14,648.5, respectively.

Table 5.3: Simulated spectral features at the desired modes traveling through the four output ports of the MDM multiplexing at λ=1565.66 nm.

Channel Number	FWHM (nm)	Finesse	Q factor
TE_0 at output port1	0.11	78.27	14,234
TE_1 at output port2	0.12	71.75	13,048
TE_2 at output port3	0.10	86.1	15,656
TE_3 at output port4	0.10	86.1	15,656

5.2.4 Inter-modal Crosstalk

From the spectral transmission of each mode depicted in Figs. 5.5 to 5.7, we can compute the level of optical inter-modal crosstalk. Figure 5.5 shows the transmission spectrum at the output port of the second ring, which includes the TE_0 and TE_1 modes, where the crosstalk is -34.47 dB at λ =1565.66 nm. Likewise, the output port of the third ring supports the TE_0, TE_1, and TE_2, where the maximum crosstalk is -29.4 dB between the TE_1 and TE_2 modes, as shown in Fig. 5.6. Lastly, the fourth multimode output port guides TE_0, TE_1, TE_2, and TE_3, in which the maximum crosstalk is reached at -30.89 dB between TE_2 and TE_3. This is illustrated in Fig. 5.7 which shows that the minimum crosstalk is -67.99 dB between the TE_0 and TE_3 modes at the last output port. Further details are provided in Table 5.4.

Table 5.4: Simulated inter-modal crosstalk feature between the modes traveling in the same multimode output port at λ=1565.66 nm.

Output Port Number	TE_0-TE_1 (dB)
Output port2	-34.47

Output Port Number	TE_0-TE_2 (dB)	TE_1-TE_2 (dB)
Output port3	-50.12	-29.4

Output Port Number	TE_0-TE_3 (dB)	TE_1-TE_3 (dB)	TE_2-TE_3 (dB)
Output port4	-67.99	-34.27	-30.89

5.2.5 Taper Spectrum

The MDM multiplexer design comprises a single bus waveguide made by implementing linear tapered waveguides between the drop bus waveguides of the different ring resonators. The linear tapers were modeled with ANSYS Lumerical MODE EME solver. One challenge is to optimize the length of the tapers to properly confine the propagating modes in order to minimize optical loss and inter-modal crosstalk. Therefore, in this design, TE_0, TE_1, and TE_2 should be transported without loss to the output port. After scanning the taper length, it was shown that a minimum length of 10 μm provides low losses and crosstalk while keeping the device compact. The spectral transmission of the third taper guiding three modes is provided in Fig. 5.8, showing a normalized transmission of up to 0.99 for the modes traveling through the tapered waveguide. Furthermore, the tapered waveguide widths are defined based on the width of the different sections of the multimode drop bus waveguide.

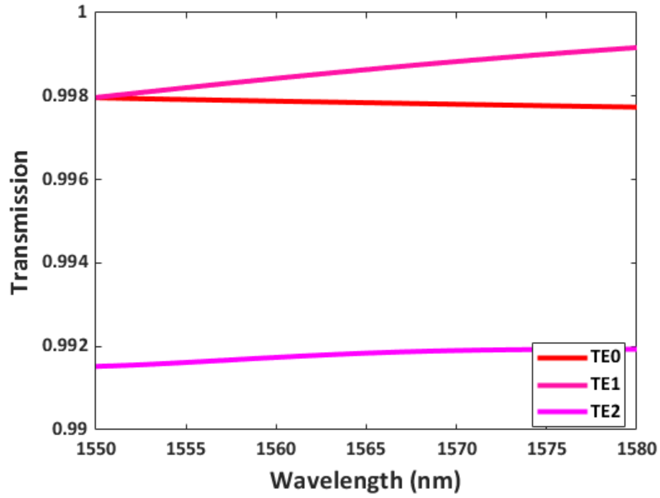

Figure 5.8: Simulated spectral transmission for the 3^{rd} taper, which supports three modes: TE_0, TE_1, and TE_2.

5.3 Conclusion

This chapter presented the design and simulation results of a four-channel MDM multiplexer based on silicon racetrack resonators. This approach was modeled using the same method as in the previous chapter, at room temperature. This multiplexer displays good optical characteristics such as low crosstalk, low insertion loss, a narrow 3-dB bandwidth, and a high Q factor. We showed that the same coupling coefficients are not required for the asymmetric racetrack resonator to perform the mode conversion process.

Chapter 6

Temperature Dependency

In this chapter, the optical characteristics of the simulated four-channel ring-based WDM and MDM multiplexers are analyzed as a function of environmental temperature variations to determine which multiplexing technique is most sensitive to thermal changes. The results in this chapter are functions of wavelength and temperature in order to show how the micro-ring and racetrack resonator behavior is affected by temperature changes. Changing the temperature essentially leads to a change in the effective index of the mode, resulting in a wavelength shift. Notably, rings are extremely sensitive to thermal variations. Furthermore, silicon has a high thermo-optic coefficient. Therefore, this sensitivity to temperature can be a serious limitation to the deployment of silicon photonics in harsh environments. Nevertheless, the need for affordable high-capacity interconnects for these environments is growing. Hence, the study presented in this chapter is investigating which of the multiplexing techniques and devices presented in chapters 4 and 5 suffer the most performance degradation when the temperature changes. Accordingly, we swept the temperature from 25 $^{\circ}C$ to 75 $^{\circ}C$ in steps of 10 $^{\circ}C$ in the simulation models introduced in the previous chapters. The results of these simulations are presented and analyzed in the following sections.

6.1 Effect of Temperature on the Resonant Wavelengths

The wavelength shift caused by changes in temperature was investigated for both multiplexer designs. According to the simulated response, the resonant wavelength of both the WDM and MDM multiplexers shifts by 0.078 $nm/^{\circ}C$. Despite the difference between the WDM and MDM multiplexers, described in Chapters 4 and 5, and the different insertion loss levels, the two designs show the same shift in resonant wavelength. This is because both approaches have the same initial effective index of 2.27. Another important point is that inside the resonators the light is always traveling in the fundamental mode in both devices. Therefore, the resonant wavelength shift is not mode dependent. Figure 6.1 shows the wavelength shift occurring in the first channel of the WDM multiplexer and in the last channel of the MDM multiplexer (i.e., the one corresponding to the TE_3 mode). Both show the same shift but the MDM multiplexer suffers from higher losses.

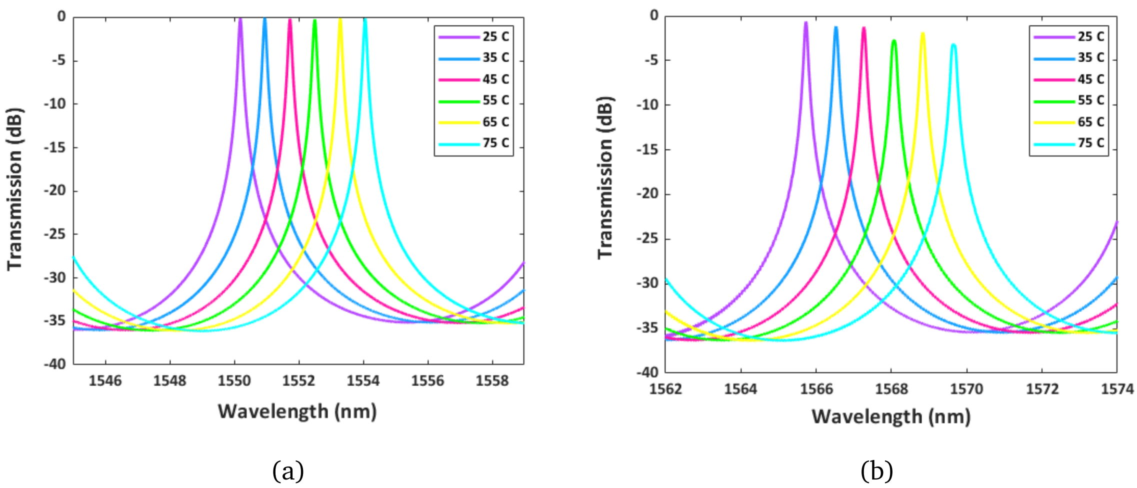

Figure 6.1: Spectra showing the resonant wavelength shift due to the temperature changes (a) for the 1^{st} channel in the WDM demultiplexer and (b) for the TE_3 mode channel in the MDM multiplexer.

6.2 Effect of Temperature on the Coupling Coefficients

Figure 6.2 shows the coupling coefficients as a function of temperature for the first channel of WDM multiplexer at λ=1550.18 nm and for the fourth channel of the MDM multiplexer at λ=1565.66 nm. In both cases, k_1 and k_2 decrease slightly as the temperature increases. However, the simulated results show that k_1 has more variation than k_2. Accordingly, k_1 decreases by 0.09% and 0.13% in the WDM and MDM multiplexers, respectively, from 25 $°C$ to 75 $°C$. Moreover, the average rate of change as a function of temperature of k_1 and k_2 is 0.0018 %/$°C$ and 0.0015 %/$°C$ in the WDM whereas, it is 0.0026 %/$°C$ and 0.0013 %/$°C$ in the MDM multiplexer.

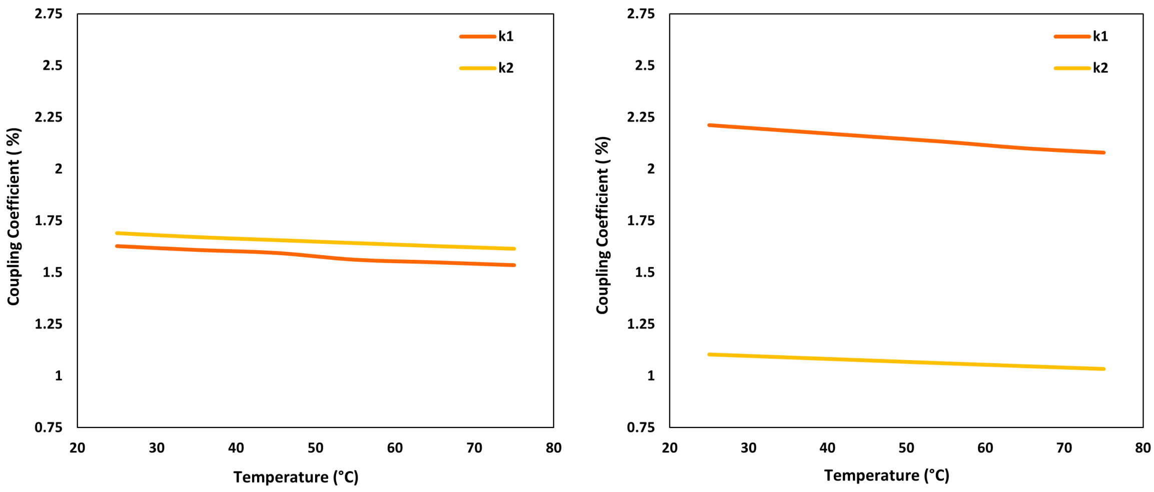

(a) (b)

Figure 6.2: Coupling coefficients vs.temperature (a) for the 1^{st} channel in the WDM demultiplexer and (b) for the TE_3 mode channel in the MDM multiplexer.

6.3 Effect of Temperature on the Transmission and Loss

This section describes the effects of thermal variations on the drop port transmission and insertion loss of both approaches. Their variations as a function of temperature are plotted in Fig. 6.3. As indicated in (c) and (d), the transmission and insertion loss of the MDM multiplexer show higher sensitivity to variations in temperature. Moreover, there are clean trends across all channels: the transmission efficiency decreases with increasing temperature while the loss increases. The normalized transmission and the insertion loss vary from 0.97 to 0.48 and from 0.14 dB to 3.21 dB, respectively.

However, less variations are observed in the WDM multiplexer, as presented in Fig. 6.3(a) and (b). The transmission and insertion loss in the WDM vary from 0.99 to 0.85 and from 0.047 dB to 0.71 dB, respectively. The fact that these small variations do not show conclusive trends across channels is an indication of the limit in accuracy of the numerical simulations. This limited accuracy affects the results in two ways: obviously, it introduces uncertainty in the transmission and loss values, but it also constrains the precision with which the design of the devices can be optimized. For instance, the transmission of the fourth channel drops with temperature while the one of the second channel slightly increases. This shows that the parameters of the second channel (i.e., ring radius and coupler gap) could be marginally improved. Nevertheless, variations of less than 10% in normalized transmission and of less than 0.5 dB in loss are challenging to measure experimentally and these uncertainty values are in agreement with the ones observed in the simulation results.

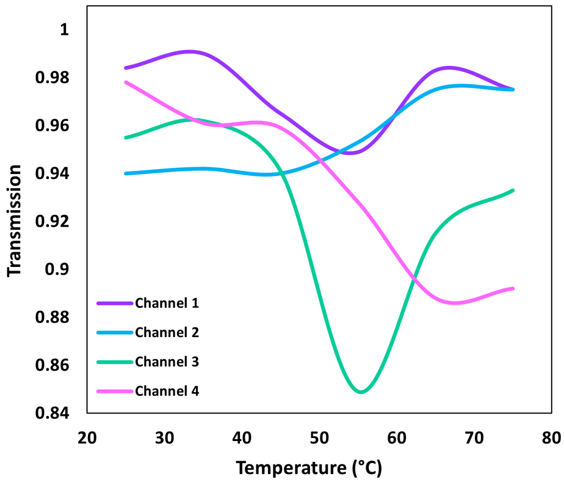

(a)

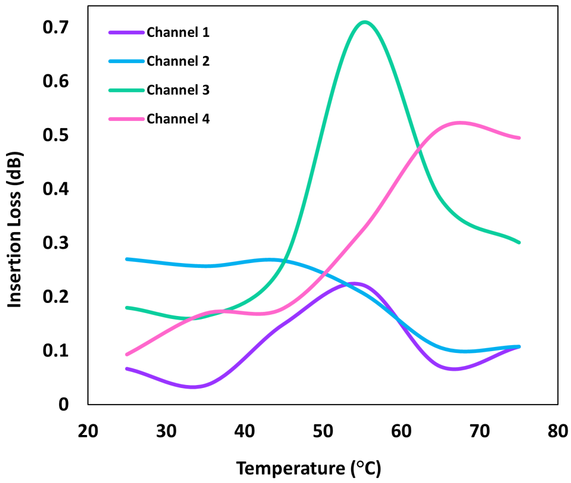

(b)

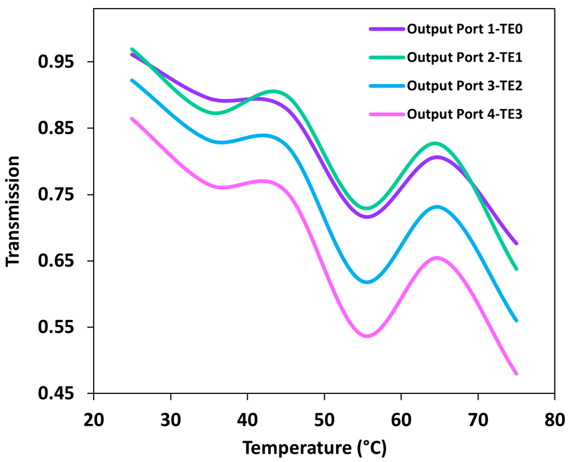

(c)

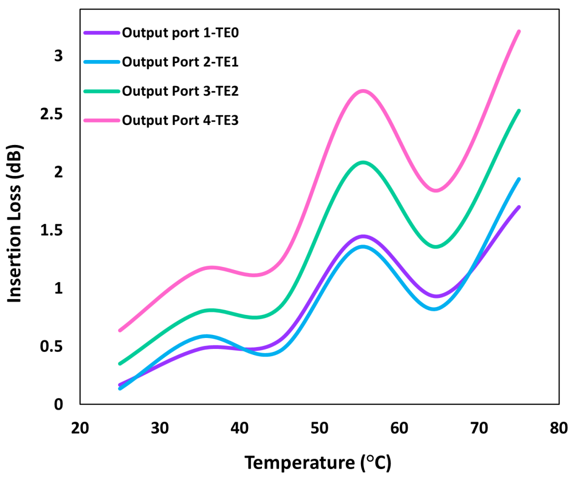

(d)

Figure 6.3: Impact of temperature variations on (a) the drop port normalized transmission intensity and (b) insertion loss for the four wavelength channels of the WDM multiplexer and on (c) the drop port normalized transmission intensity and (d) insertion loss for the four mode channels of the MDM multiplexer.

Furthermore, this sensitivity to variations in temperature leads to a slight enhancement in the 3-dB bandwidth that, in turn, causes a decrease in Q factor. The temperature variation from 25 $^{\circ}C$ to 75 $^{\circ}C$ increases the WDM and MDM devices 3-dB bandwidth to 0.11 nm and 0.17 nm, respectively. Thus, achieving a consistent Q factor is not straightforward, especially with the MDM approach.

6.4 Effect of Temperature on the Extinction Ratio

This section addresses the effect of thermal changes on the extinction ratio of both multiplexers. Figure 6.4 presents the variation in ER as a function of temperature. In this study, the drop port ER varies from 35.87 dB to 37.73 dB in the WDM multiplexer and from 35.67 dB to 31.61 dB in MDM multiplexer. Since the signals at the output of the through port are very low when the rings are on resonance (below 0.02 in normalized power), the variations in ER at the through port are not discussed here.

Figure 6.4(a) shows the ER as a function of temperature for the four channels of the WDM multiplexer. The ER varies by less than one dB over the full temperature range. However, in the case of the MDM multiplexer the ER decreases as the temperature increases, as shown in Fig. 6.4(b). The reduction in ER is a consequence of the lower transmission efficiency and higher loss as a function of temperature described in the previous section (see Fig. 6.3(c) and (d)). When less light is transmitted, then the ER decreases. Indeed, one can see that the shape of the curves in Figs. 6.3(c) and 6.4(b) are similar.

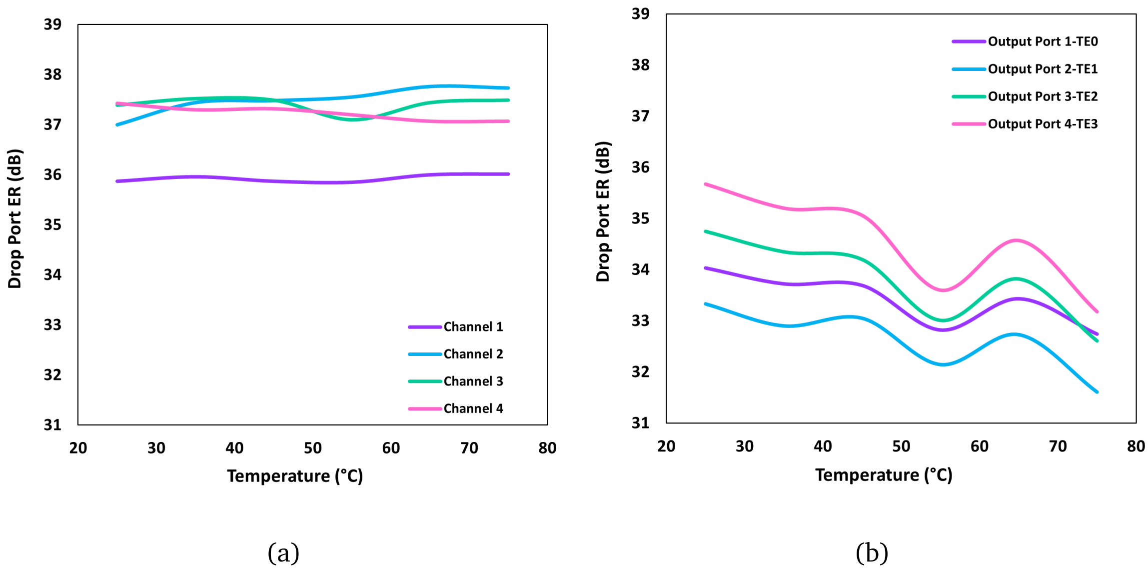

Figure 6.4: Impact of temperature variations on the drop port extinction ratio (ER) for each channel of (a) the WDM demultiplexer and (b) the MDM multiplexer.

6.5 Effect of the Temperature on the Crosstalk

Figure 6.5 presents the main source of crosstalk as a function of temperature relative in both multiplexers. Figure 6.5(a) shows the adjacent channel crosstalk between the four channels in the WDM demultiplexer, and (b) shows inter-modal crosstalk between the four different modes at the output port of the MDM multiplexer for a single wavelength. The simulations demonstrate that crosstalk is not strongly dependent on temperature. In this study, the maximum crosstalk fluctuation is 1.07 dB between the first and second channels of the WDM demultiplexer and 0.89 dB between the TE_0 and TE_3 modes in the MDM multiplexer.

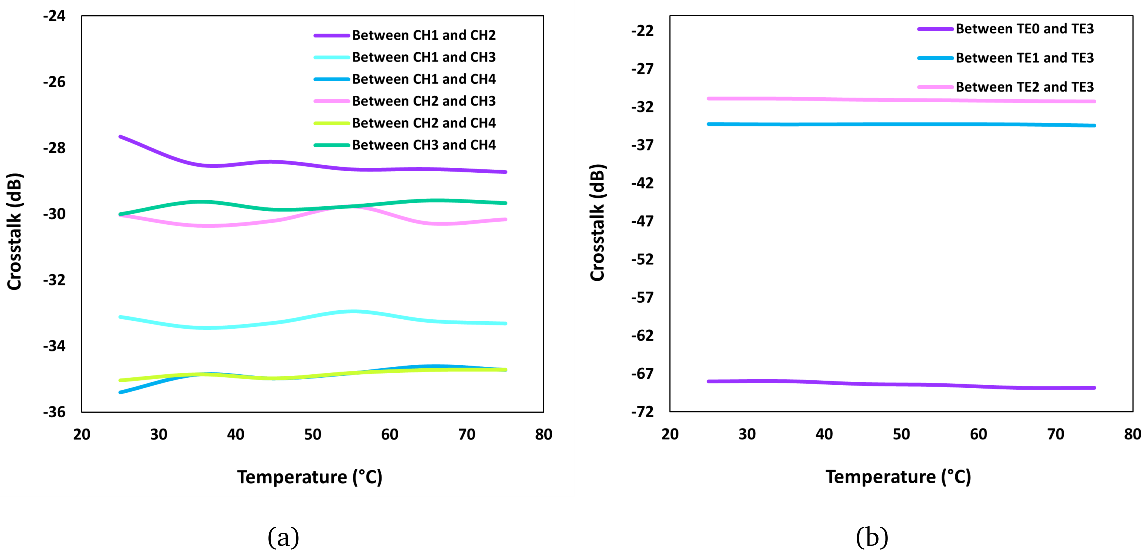

Figure 6.5: Impact of temperature variations (a) on the adjacent channel crosstalk in the WDM demultiplexer and (b) on the inter-modal crosstalk in the MDM multiplexer.

6.6 Conclusion

This chapter presented the effect of thermal variations on the optical performance of the two simulated multiplexers. The results demonstrated that the coupling coefficients vary slightly with temperature. Moreover, since the fundamental mode inside the rings of the two devices has the same effective index, both demonstrated the same resonant wavelength shift as a function of temperature. Furthermore, the level of crosstalk barely changed with temperature in both devices. However, there is a significant difference in the behavior of the insertion loss as a function of temperature between the devices. Losses increase much more with temperature in the

MDM multiplexer than in the WDM one. The same trend was also observed with regards to the extinction ratio. This is the key finding of this study. The higher thermal sensitivity of the MDM device is most likely due to the racetrack resonator configurations that results in significantly longer coupling regions. Moreover, for the higher-order modes different couplers are used at the input and output of the rings, which will further enhance the temperature sensitivity. The racetrack configuration was chosen to obtain the level of coupling required to achieve the critical coupling condition with the higher-order modes. Therefore, minimizing the length of the couplers needed to perform mode conversion in micro-rings appears to be critical to reduce the sensitivity to temperature of MDM multiplexer. Eventually, since the filtering is done with similar single mode rings in the MDM approach, all modes in the similar multimode waveguide have comparable resonant wavelength shift, ER, FWHM, and Q factor.

Chapter 7

Conclusion

This thesis presented the design and simulation of two silicon photonic multiplexers based on micro-ring resonators. The first device was a four channel WDM demultiplexer design to work on the 200 GHz grid defined by the ITU. Only the fundamental TE mode is supported inside this device. The second device, a MDM multiplexer, is able to support four TE modes and each mode represents a different telecommunication channel. One important advantage of the MDM technique is that a single source can be used for its implementation whereas WDM requires multiple sources.
Both multiplexers have the same effective index for the fundamental mode of the micro-rings and thereby they experienced the same resonant wavelength shift as a function of temperature. This study shows that despite suffering from similar shifts in wavelength due to variations in temperature, the longer directional couplers (DC) used to perform mode conversion in the MDM multiplexer make its performance more sensitive to changes in temperature. Also, for the higher-order modes, the fact that different DCs are used at the input and output of the resonators can contribute to the temperature sensitivity. Controlling thermal drift in the MDM multiplexer will be more challenging than in WDM systems since the coupling ratio provided by the DC as well as the phase must be accurately tuned, whereas in WDM, the fact that both DC are identical means that only the phase requires fine adjustments. We also showed that a ring resonator with high insertion loss is more sensitive to the thermal effects. These results were presented at the Photonics North Conference.

To continue the investigation started in this thesis, future work could include the fabrication and characterization of the multiplexers to confirm the simulation results. More research could also be done to improve the temperature sensitivity of the directional couplers used to perform mode conversion in the MDM device.

Bibliography

Mulcahy, J., Peters, F. H., & Dai, X. (2022, January). Modulators in Silicon Photonics—Heterogenous Integration & and Beyond. In Photonics (Vol. 9, No. 1, p. 40). Multidisciplinary Digital Publishing Institute.

Yuan, Y., Tossoun, B., Huang, Z., Zeng, X., Kurczveil, G., Fiorentino, M., ... & Beausoleil, R. G. (2021). Avalanche photodiodes on silicon photonics. Journal of Semiconductors, 43, 1-13.

Yan, S., Adcock, J., & Ding, Y. (2021). Graphene on Silicon Photonics: Light Modulation and Detection for Cutting-Edge Communication Technologies. Applied Sciences, 12(1), 313.

Besancon, C., Néel, D., Make, D., Ramírez, J. M., Cerulo, G., Vaissiere, N., ... & Decobert, J. (2021). AlGaInAs Multi-Quantum Well Lasers on Silicon-on-Insulator Photonic Integrated Circuits Based on InP-Seed-Bonding and Epitaxial Regrowth. Applied Sciences, 12(1), 263.

Gautam, R. (2014). Silicon microring resonator loaded mach-zehnder interferometer for low power optical modulation, switching and bio-sensing.

Chang, L., Cole, G. D., Moody, G., & Bowers, J. E. (2022). CSOI: Beyond Silicon-on-Insulator Photonics. Optics and Photonics News, 33(1), 24-31.

Mistry, A. (2020). Silicon-on-insulator, free-spectral-range-free devices for wavelength-division multiplexing applications (Doctoral dissertation, University of British Columbia).

Zheng, Y., Lia, Y., Yan, Y., Zhang, P., & Duan, J. A. (2022). Compact low-loss low-crosstalk echelle grating demultiplexer on silicon-on-insulator for CWDM. Optik, 249, 168236.

Liu, J., Cristoloveanu, S., & Wan, J. (2021). A Review on the Recent Progress of Silicon-on-Insulator-Based Photodetectors. physica status solidi (a), 218(14), 2000751.

Sayed, A. F., Mustafa, F. M., Khalaf, A. A., & Aly, M. H. (2021). Symmetrical and post dispersion compensation in WDM optical communication systems. Optical and Quantum Electronics, 53(1), 1-19.

Rai, S., & Garg, A. K. (2021). Analysis of RWA in WDM optical networks using machine learning for traffic prediction and pattern extraction. Journal of Optics, 1-8.

Bagheri, S., & Green, W. M. (2009, September). Silicon-on-insulator mode-selective add-drop unit for on-chip mode-division multiplexing. In 2009 6th IEEE International Conference on Group IV Photonics (pp. 166-168). IEEE.

Zheng, S., Cao, X., & Wang, J. (2018, May). Demonstration of microring-based WDM-compatible mode-division multiplexing on a silicon chip. In CLEO: Science and Innovations (pp. JW2A-12). Optical Society of America.

Qiu, Y., Li, X., Luo, M., Chen, D., Wang, J., Xu, J., ... & Yu, S. (2017). Mode-selective wavelength conversion of OFDM-QPSK signals in a multimode silicon waveguide. Optics express, 25(4), 4493-4499.

Li, C., Liu, D., & Dai, D. (2019). Multimode silicon photonics. Nanophotonics, 8(2), 227-247.

Ding, Y., Xu, J., Ou, H., & Peucheret, C. (2014). Mode-selective wavelength conversion based on four-wave mixing in a multimode silicon waveguide. Optics express, 22(1), 127-135.

Jia, H., Fu, X., Zhou, T., Zhang, L., Yang, S., & Yang, L. (2019). Mode-selective modulation by silicon microring resonators and mode multiplexers for on-chip optical interconnect. Optics Express, 27(3), 2915-2925.

Luo, L. W., Ophir, N., Chen, C. P., Gabrielli, L. H., Poitras, C. B., Bergmen, K., & Lipson, M. (2014). WDM-compatible mode-division multiplexing on a silicon chip. Nature communications, 5(1), 1-7.

Zhou, D., Yu, Y., Yu, Y., & Zhang, X. (2018). Parallel radio-frequency signal-processing unit based on mode multiplexed photonic integrated circuit. Optics Express, 26(16), 20544-20549.

Rohit, G., Heebner, J., & Ibrahim, T. (2008). Optical microresonators. Optical Microresonators: theory, fabrication, and applications, 1-2.

Okamoto, K.(2021). Fundamentals of optical waveguides. Elsevier.

Steck, D. A. (2006). Classical and modern optics. Oregon University.

Bogaerts, W., De Heyn, P., Van Vaerenbergh, T., De Vos, K., Kumar Selvaraja, S., Claes, T., ... & Baets, R. (2012). Silicon microring resonators. Laser & Photonics Reviews, 6(1), 47-73.

Ding, Y., Xu, J., Ou, H., & Peucheret, C. (2014). Mode-selective wavelength conversion based on four-wave mixing in a multimode silicon waveguide. Optics express, 22(1), 127-135.

Li, G., Bai, N., Zhao, N., & Xia, C. (2014). Space-division multiplexing: the next frontier in optical communication. Advances in Optics and Photonics, 6(4), 413-487.

Pollock, C. R., & Lipson, M. (2003). Integrated photonics (Vol. 20, No. 25, p. 30).

Bogaerts, W., & Chrostowski, L. (2018). Silicon photonics circuit design: methods, tools and challenges. Laser & Photonics Reviews, 12(4), 1700237.

Mansoor, R. D., Sasse, H., Al-Asadi, M., Ison, S. J., & Duffy, A. P. (2015). Estimation of the bandwidth of acceptable crosstalk of parallel coupled ring resonator add/drop filters. IEEE Transactions on Electromagnetic Compatibility, 57(5), 1005-1012.

Mansoor, R., Koziel, S., Sasse, H., & Duffy, A. (2015). Crosstalk suppression bandwidth optimisation of a vertically coupled ring resonator add/drop filter. Iet Optoelectronics, 9(2), 30-36.

Mansoor, R. D., Sasse, H., Al Asadi, M., Ison, S. J., & Duffy, A. P. (2014). Over coupled ring resonator-based add/drop filters. IEEE Journal of Quantum Electronics, 50(8), 598-604.

Bahadori, M., Rumley, S., Jayatilleka, H., Murray, K., Jaeger, N. A., Chrostowski, L., ... & Bergman, K. (2016). Crosstalk penalty in microring-based silicon photonic interconnect systems. Journal of Lightwave Technology, 34(17), 4043-4052.

Wang, J. (2016). Grating and ring based devices on SOI platform. McGill University (Canada).

Mansoor, R. (2015). Crosstalk and Signal Integrity in Ring Resonator Based Optical Add/Drop Multiplexers for Wavelength-Division-Multiplexing Networks.

Yen, T. H., & Hung, Y. J. (2020). Fabrication-tolerant CWDM (de) multiplexer based on cascaded Mach–Zehnder interferometers on silicon-on-insulator. Journal of Lightwave Technology, 39(1), 146-153.

Zhang, Z., Huang, B., Zhang, Z., Chen, C., Mao, X., Liu, S., & Chen, H. (2015, August). A WDM silicon photonic transmitter based on Mach-Zehnder modulator with surface-normal optical interface. In 2015 IEEE 12th International Conference on Group IV Photonics (GFP) (pp. 79-80). IEEE.

Tan, D. T. H., Grieco, A., & Fainman, Y. (2014). Towards 100 channel dense wavelength division multiplexing with 100GHz spacing on silicon. Optics express, 22(9), 10408-10415.

Uddin, M. R., Masri, N. M. H., & Ahsan, M. S. (2021, September). Photonic Microring Resonator Based DWDM System Within a Single Free Spectral Range. In 2021 International Conference on Electronics, Communications and Information Technology (ICECIT) (pp. 1-5). IEEE.

Jia, H., Fu, X., Zhou, T., Zhang, L., Tian, Y., Yang, S., & Yang, L. (2019). Interface of electrical data-bus to multimode optical data-bus using racetrack microring resonators. IEEE Photonics Technology Letters, 31(17), 1397-1400.

Qiu, Y., Li, X., Luo, M., Chen, D., Wang, J., Xu, J., ... & Yu, S. (2017). Mode-selective wavelength conversion of OFDM-QPSK signals in a multimode silicon waveguide. Optics express, 25(4), 4493-4499.

Nath, J. P., Dhingra, N., Saxena, G. J., & Sharma, E. K. (2020). Compact mode division (de) Multiplexer based on collaterally coupled SOI waveguides. IEEE Photonics Technology Letters, 32(10), 595-598.

Bogaerts, W., De Heyn, P., Van Vaerenbergh, T., De Vos, K., Kumar Selvaraja, S., Claes, T., ... & Baets, R. (2012). Silicon microring resonators. Laser & Photonics Reviews, 6(1), 47-73.

Rouger, N., Chrostowski, L., & Vafaei, R. (2010). Temperature effects on silicon-on-insulator (SOI) racetrack resonators: A coupled analytic and 2-D finite difference approach. Journal of Lightwave Technology, 28(9), 1380-1391.

Liu, W., Li, M., Chang, W., Xiao, C., Xie, Y., Guan, N., & Jiang, L. (2019, March). Thermal sensing using micro-ring resonators in optical network-on-chip. In 2019 Design, Automation & Test in Europe Conference & Exhibition (DATE) (pp. 1611-1614). IEEE.

Li, S., Nong, Z., Wu, X., Yu, W., He, M., Klitis, C., ... & Cai, X. (2018). Orbital angular momentum vector modes (de) multiplexer based on multimode micro-ring. Optics express, 26(23), 29895-29905.

De Cea, M., Atabaki, A. H., & Ram, R. J. (2019). Power handling of silicon microring modulators. Optics express, 27(17), 24274-24285.

Wu, D., Wu, Y., Wang, Y., An, J., & Hu, X. (2016). Reconfigurable optical add-drop multiplexer based on thermally tunable micro-ring resonators. Optics Communications, 367, 44-49.

De Heyn, P., De Coster, J., Verheyen, P., Lepage, G., Pantouvaki, M., Absil, P., ... & Van Thourhout, D. (2013). Fabrication-tolerant four-channel wavelength-division-multiplexing filter based on collectively tuned Si microrings. Journal of lightwave technology, 31(16), 3085-3092.

Huang, Q., Xiao, X., Li, Y., Li, Z., Yu, Y., & Yu, J. (2009, October). Flat-top passband filter based on parallel-coupled double microring resonators in silicon. In Photonics and Optoelectronics Meetings (POEM) 2009: Optoelectronic Devices and Integration (Vol. 7516, p. 751607). International Society for Optics and Photonics.